Widespread wildfires in the early Cretaceous of China linked to angiosperm radiation and early Albian Ocean Anoxic Event 1b

Xiaotao Xu[a, b], Longyi Shao[a, *], Kenneth A. Eriksson[c], Jiamin Zhou[a], Dongdong Wang[d], Haihai Hou[e], Jason Hilton[f], Shuai Wang[e], Jing Lu[a], Timothy P. Jones[g]

[a] College of Geoscience and Surveying Engineering, China University of Mining and Technology (Beijing), Beijing 100083, China

[b] Shandong Key Laboratory of Depositional Mineralization & Sedimentary Mineral, Shandong University of Science and Technology, Qingdao 266590, China

[c] Department of Geosciences, Virginia Tech, Blacksburg, Virginia 24061, USA

[d] College of Earth Science and Engineering, Shandong University of Science and Technology, Qingdao 266590, China

[e] College of Mining, Liaoning Technical University, Fuxin 123000, China

[f] School of Geography, Earth and Environmental Sciences, University of Birmingham, Edgbaston, Birmingham, B15 2TT, UK

[g] School of Earth and Environmental Sciences, Cardiff University, Cardiff, CF10, 3YE, Wales, UK

*** Correspondence author**

E-mail address: ShaoL@cumtb.edu.cn

Abstract

Wildfires are an important source of disturbances in the Earth system and are of great significance for understanding the interactions between environmental, atmospheric and vegetation changes over deep time. The early Cretaceous was a “high-fire” interval with frequent and widespread wildfires globally, but the timing and global significance of wildfire events during this time remain uncertain. We undertake a multi-proxy study evaluating kerogen macerals, inertinite reflectance, and polycyclic aromatic hydrocarbons (PAHs) from mudstones

to characterize wildfire activity in the Albian coal-forming Fuxin lacustrine Basin, and correlate these with (i) environmental and floral changes on land, and (ii) well-dated marine events including the early Albian Oceanic Anoxic Event 1b (OAE 1b), to consider their environmental and climatic significance. The presence of high inertinite contents demonstrate that multiple, widespread wildfire events occurred during the early Albian, which are correlated stratigraphically to the Kilian, Paquier and Leenhardt sub-events of the early Albian OAE 1b. Inertinite reflectance values ranging from 0.6% to 3.8%Ro show that wildfires in the early Albian were dominated by ground fires, with a smaller proportion of surface fires and almost no crown fires. Atmospheric oxygen concentration (pO_2) levels, estimated from inertinite contents, attained ~25% during the early Albian, which exceeded the present atmospheric oxygen level of 21% and was able to support sustained combustion. Climate conditions and frequent wildfire activity in the early Albian acted as an important control on vegetation distribution and diversification, which further promoted the evolution of early angiosperms in early Cretaceous landscapes. Wildfire activity resulted in the burning and destruction of both vegetation and soil structure, enhancing the post-fire erosion associated with intensified continental weathering under warmer and more humid conditions during the early Albian OAE 1b interval. These episodes of high wildfire activity correlate with high nutrients and organic matter levels in lakes and thereby contributed to eutrophication and anoxia in lacustrine and in contemporaneous oceanic systems.

Keywords

Cretaceous; early Albian; Fuxin Basin; wildfires; inertinite; Ocean Anoxic Event 1b

1. Introduction

Wildfires have played an important role in Earth system changes since the Silurian period when land plants first appeared on Earth and profoundly influenced global ecosystem patterns and processes (Glasspool et al., 2004; Glasspool et al., 2015; Lu et al., 2021). Charcoal, as the byproduct of wildfires, is recorded from the late Silurian (~420 Ma) to the present (Scott and Glasspool, 2006) and provides evidence for wildfire events in the rock record (Scott and Glasspool, 2007; Scott, 2010; Shao et al., 2012; Wang et al., 2019a; Wang et al., 2021a).

Fusinite and semifusinite, the most frequent members of the inertinite maceral group, are believed to be the product of incomplete combustion from wildfires and were regarded as fossil charcoal in previous studies (e.g., Bustin and Guo, 1999; Scott, 2002). Some maceral formation mechanisms in inertinite, such as macrinite, may be related to fungal and/or bacterial degradation and/or arthropod ingestion and excretion (Hower et al., 2013). Although the origin of inertinite is still under frequent debate, more recent studies have concluded that inertinite is synonymous with charcoal and is almost exclusively considered as the byproduct of wildfires (e.g., Scott and Glasspool, 2007; Diessel, 2010; Glasspool and Scott, 2010; Glasspool et al., 2015). Inertinite is common throughout much of the Cretaceous Period (Diessel, 2010; Wang et al., 2021a), and recent evidence indicates widespread and frequent wildfires occurred during the Cretaceous (Bond and Scott, 2010; Brown et al., 2012; Sender et al., 2014; Moore et al., 2021; Wang et al., 2019b, 2021b). Thus, the Cretaceous has been considered as a "high-fire" world (Brown et al., 2012).

Polycyclic Aromatic Hydrocarbons (PAHs) in sediments are a powerful proxy for the identification of wildfire process throughout geologic history (e.g., Grice et al., 2007; Marynowski and Simoneit, 2009; Zakir Hossain et al., 2013; Zhou et al., 2021). Numerous studies have shown that unsubstituted PAHs, mostly consisting of 3–6 rings, can be used to indicate pyrogenic sources from combustion of organic matter (Page et al., 1999; Liu et al., 2005; Denis et al., 2012; Xu Y, et al., 2020a). High levels of PAHs are noted in various Cretaceous successions adding further support to the Cretaceous being a "high fire" interval (Finkelstein et al., 2005; Boudinot and Sepúlveda, 2020).

Wildfires respond strongly to atmospheric oxygen concentration (pO_2), and variations in the occurrence and abundance of inertinite in the Earth's history have been used to estimate pO_2 levels (Jones and Chaloner, 1991; Wildman et al., 2004; Belcher et al., 2010; Glasspool and Scott, 2010; Shao et al., 2012; Glasspool et al., 2015; Hou et al., 2020; Wang et al., 2021a). Related studies have revealed that pO_2 above the present-day level of 21% would enable fuels to burn more frequently, while pO_2 levels below 18.5% would suppress fire frequency (Belcher et al., 2010). Wildfire is a significant evolutionary force that has shaped global biome distribution through geological time, and increased wildfire activity has been linked to the abundance of gymnosperms and the emergence of angiosperms (Bond and Scott,

2010; Brown et al., 2012). Conifer forests were abundant throughout the Cretaceous Period (e.g., Harland et al., 2007; Friis et al., 2010) from which wildfires have been hypothesized as opening up Cretaceous forests and promoting the expansion of early angiosperms (Bond and Scott, 2010; Belcher and Hudspith, 2016). Additionally, direct and indirect evidence shows that angiosperms created novel wildfire regimes with positive feedbacks leading to more frequent wildfires, which would have facilitated their further diversification and spread (Bond and Scott, 2010; Belcher and Hudspith, 2016; Belcher et al., 2021).

The early Albian Oceanic Anoxic Event 1b (OAE 1b) has been widely identified in multiple marine organic-rich sedimentary successions and carbon isotope excursions (Trabucho Alexandre et al., 2011; Coccioni et al., 2014) that represent major disturbances in the global carbon cycle (Jenkyns, 2010). The phenomenon of increased inertinite contents at the onset of Oceanic Anoxic Events (OAEs) has also been observed (Baker et al., 2017), which has provided evidence for enhanced wildfire activity in terrestrial settings during the OAEs onset. According to the model of Handoh and Lenton (2003), increased organic carbon burial across OAEs would have led to a gradual rise in pO_2 level and an increase in wildfire activity. Wildfires can result in the burning and destruction of land surface vegetation and soil structures (Brown et al. 2012), which increases the erosion potential and the flux of terrestrial organic matter and nutrients into the oceans, contributing to oceanic planktonic blooms and associated anoxic events (Brown et al. 2012; Glasspool et al., 2015; Yan et al., 2019; Xu et al., 2020a).

Numerous past studies have focused on sedimentary environments, palaeontology, tectonic evolution and coal accumulation in the Lower Cretaceous continental coal-bearing series of the Fuxin Basin (e.g., Chen et al., 1981; Guo, 1988; Liu et al., 1992; Wang et al., 1998; Zhu et al., 2007; Cai et al., 2011; Xu et al., 2020b), making these continental strata ideal for analyzing palaeoclimate and palaeoenvironmental changes during this time. Nevertheless, few studies have focused on wildfire activity in the Lower Cretaceous, and the possible relationships between wildfires, plant evolution, and anoxic events. In this paper, we conduct analyses of kerogen macerals, inertinite reflectance, PAHs of mudstones from the early Cretaceous Shahai and Fuxin formations in the Fuxin Basin. Based on these data, we identify wildfire records and wildfire types, and attempt to estimate pO_2 levels from inertinite contents and to interpret the role of wildfires not only on plant evolution, but also on the early Albian

OAE 1b. This is important for linking synchronous environmental changes on land and in the oceans to better understand their relationships with one another.

2. Geological setting

The continental Fuxin Basin is located in western Liaoning Province, northeastern China, on the northeastern part of the North China Plate (NCP) (Fig. 1a, b; Zhu et al., 2007). During the Jurassic–Cretaceous, the northeastern NCP was located in a back-arc setting and strongly influenced by subduction of the Palaeo-Pacific Plate (Fig. 1c; e.g., Zhu et al., 2017; Su et al., 2021). The Lower Cretaceous represents a peak period of rifting and magmatism in the northeastern NCP (Wu et al., 2014; Zhu et al., 2017). The Fuxin Basin is a fault-bounded basin that formed from rifting in the late Jurassic to early Cretaceous (Liu et al., 1992; Wang et al., 1998). The basin is bounded by the Lvshan Fault to the east and the Songling Fault to the west (Zhu et al., 2007), and extends from Shala city in the north to the Dalinghe Fault in the south (Fig. 2a). During the early Cretaceous the Fuxin Basin was at a palaeolatitude of ~40–45°N (Zhou et al., 2003; Li and Jiang, 2013).

The Lower Cretaceous sedimentary rocks in the Fuxin Basin comprise the Yixian, Jiufotang, Shahai, Fuxin, and Sunjiawan formations from oldest to youngest (Fig. 2b; Wan et al., 2013). In this study, the Shahai and Fuxin formations were selected to investigate continental wildfire records. The Shahai Formation mainly consists of mudstone, sandstone and conglomerate, with minor coal seams developed that were deposited in a continually expanding lacustrine basin (Zhu et al., 2007). From the bottom to the top, the Shahai Formation is subdivided into four members according to their lithological association (Li, 1988). The first and second members are mainly composed of conglomerates and coarse-grained sandstones that formed in an alluvial fan depositional system. The third member predominantly consists of sandstones and coal seams and formed in fan delta and lacustrine depositional systems. The fourth member is composed of thick-bedded black mudstones and fine-grained sandstones and is dominated by lacustrine depositional systems (Fig. 3; Guo, 1988; Zhu et al., 2007; Cai et al., 2011). The Fuxin Formation is predominantly composed of sandstones and mudstones with coal seams. It was deposited in fluvial and swamp sedimentary environments (Fig. 3; Xu et al., 2020b).

U-Pb zircon ages of the Yixian Formation from volcanic samples have been dated at 131–119 Ma (Xu et al., 2012; Zhang et al., 2016; Su et al., 2021; Fig. 2). Tuff samples from the Jiufotang Formation have given ages of 121–120 Ma (He et al., 2004; Su et al., 2021; Fig. 2). Zircon U-Pb dating of the tuffaceous claystone near the bottom of the fourth member of the Shahai Formation from the DY-1 borehole (1225.5m) gave an age of 112.6 ± 1.7 Ma (Fig. 3; Xu et al., 2022). This age constrains the fourth member of the Shahai Formation to the early part of the Albian Stage. Basalt samples at the top of the Fuxin Formation have yielded $^{40}Ar/^{39}Ar$ ages between 105.5 and 102.2 Ma (Zhu et al. 2004). These isotopic ages demonstrate that the Yixian, Jiufotang, Shahai and Fuxin formations are of Lower Cretaceous age. In China, the Lower Cretaceous is divided into the Jibei, Jehol and Liaoxi regional stratigraphic stages (Wan et al., 2013). Of these, the Liaoxi regional stage includes the Shahai, Fuxin and Sunjiawan formations in ascending stratigraphic order, and contains the Fuxin flora (Fig. 2b). The Fuxin flora is dominated by ferns, Ginkgoales and conifers, with abundant cycads and Equisetales and some angiosperms. It has been divided into three floral assemblages (Deng et al. 2012) in which the composition and diversity of angiosperms increase through the early Cretaceous (Tao et al., 2013). The Shahai Formation contains the *Acanthopteris-Ginkgo coriacea* assemblage, while the lower-middle part of the Fuxin Formation contains the *Ruffordia goepperti-Dryopterites* assemblage, and the upper part of the Fuxin Formation contains the *Ctenis lyrata-Chilinia* assemblage (Deng et al. 2012). The ages of all three floral assemblages are Lower Cretaceous (Chen et al., 1988; Deng and Chen, 2001), with the Shahai and Fuxin formations dated as late Aptian to Albian in age based on biostratigraphic and lithostratigraphic correlation (Deng et al., 2012; Xi et al., 2019).

Historically, it has been difficult to correlate well-dated marine strata with continental successions. The abundance of radiometric dates from Lower Cretaceous continental strata in the NCP (Fig. 2) provide a framework for its accurate correlation with marine strata. In Lower Cretaceous marine successions, OAE 1b is recognized from the late Aptian to the early Albian (~114.5–110.5 Ma) and is subdivided into four subevents; the uppermost Aptian Jacob, and the lower Albian Kilian, Paquier and Leenhardt sub-events (Coccioni et al., 2014; Li et al., 2016; Matsumoto et al., 2020). The sub-events can be recognized from perturbations of the global carbon cycle (Herrle et al., 2004; Navarro-Ramirez et al., 2015) that can be used for

chemostratigraphy and correlation with other areas. The early Albian aged Kilian, Paquier and Leenhardt sub-events are each characterized by distinct negative carbon isotope excursions (Herrle et al., 2004; Friedrich et al., 2005; Coccioni et al., 2014), while the late Aptian aged Jacob sub-event is defined by a weak negative carbon isotope excursion within the second late Aptian positive carbon isotope excursion (Coccioni et al., 2014; Herrle et al., 2015). In the Fuxin Basin, three distinct short-term negative excursions of organic carbon isotopes ($\delta^{13}C_{org}$) are recorded during the early Albian and are inferred to represent the Kilian, Paquier and Leenhardt sub-events of the early Albian OAE 1b (Xu et al., 2022).

3. Materials and methods

Mudstone samples analyzed in this study were collected from the DY-1 borehole (41° 52' 45'' N - 121° 37' 8'' E) in the central part of the Fuxin Basin (Fig. 2a). 54 mudstone samples were collected through the Shahai and Fuxin formations (Fig. 3). All samples were collected and stored in airtight, zip-lock plastic bags to avoid oxidation and contamination. Each mudstone sample was crushed to less than 1 mm diameter and then divided into two parts. One part was used for kerogen extraction (GB/T19144-2010) which was prepared as kerogen thin sections and polished epoxy-bound blocks. Identification of kerogen macerals was determined in thin sections under transmitted and fluorescent light using a Leica DM4500P LED microscope according to the China national standard (SY/T 5125-2014), with at least 300 valid points counted for each sample. Inertinite reflectance was measured on polished blocks using a Leica DM4500P LED reflected light microscope with a ×50 oil immersion objective. For the inertinite reflectance measurements, at least 50 valid points were counted on each polished block. The remaining part of each mudstone sample was further crushed below 200 mesh (74 microns) for the analysis of PAHs. Aromatic hydrocarbon fractions were analyzed at the State Key Laboratory of Petroleum Resources and Prospecting at the China University of Petroleum in Beijing. Gas chromatography-mass spectrometry (GC-MS) analyses of the aromatic fractions were performed with an Agilent 7890GC/5975CMS following the test method for biomarkers in sediment and crude oil by GC-MS (GB/T 18606-2017). More details of the analysis method are described by Marynowski and Simoneit (2009) and Kang et al. (2020). For observation of homogenized cell walls, small mudstone fragments with charcoalified plant

fossil fragments were mounted on a standard stub, coated with gold, and then observed under a SU8020 Scanning Electron Microscopy (SEM).

4. Results

4.1 Kerogen maceral compositions

Four types of macerals, including sapropelinite, vitrinite, exinite and inertinite, were observed in the mudstone samples from the Fuxin Basin (Fig. 4). Identification results of kerogen macerals (vol.%, mmf–mineral matter free) are given in Table 1 and Fig. 3. The sapropelinite content varies from 5.1 and 52.2 vol.% with an average of 27.5 vol.%, and under transmitted light microscopy is brownish yellow with flocculent edges (Fig. 4a and 4b). Vitrinite accounts for 43.7 vol.% in average, ranging from 16.6 to 75.3 vol.%. Under transmitted light microscopy, vitrinite is brownish red and does not fluoresce under fluorescence illumination (Fig. 4c and 4d). Exinite is not commonly observed, and ranges between 0 and 24.8 vol.% with an average value of 9.3 vol.%. Exinite mainly consists of spores and pollen grains that are yellowish brown in color, fluoresce under fluorescence illumination and exhibits various monomer forms, such as round, oval and triangular shapes (Fig. 4e-j). Inertinite contents range from 8.3 to 42.5 vol.% with an average of 19.5 vol.%, typically exhibiting shapes including cubic blocks and long strips with black color and silky luster (Fig. 5a-j). Under transmitted light microscopy, inertinite entirely consists of fusinite that are pure black in color, do not fluoresce under fluorescence illumination and occur as long strips or fragmental shapes with sharp and angular edges (Fig. 4k, 4l and 4m). Under reflected light microscopy of polished blocks, inertinites shows a prominent cellular structure or compressed and broken cell walls with relatively high reflectivity (Fig. 6). Under the SEM, inertinite exhibits homogenized (stratified in life) cell walls, while some cell walls are fractured, due to the compression associated with burial (Fig. 7).

To simplify the discussion and interpretation of the inertinite results, we subdivided the change trends into four units (Fig. 3) based on their overall composition. Unit A, which developed during the early part of the late Aptian, incorporates the first and second members of the Shahai Formation and is characterized by relatively low inertinite contents between 8.3 and 15.8 vol.%, with an average of 11.6 vol.%. Unit B, which developed during the latest Aptian

represents the third member of the Shahai Formation, has an increased inertinite content that varies from 8.4 to 20.3 vol.%, with an average of 12.9 vol.%. Unit C, which developed during the early Albian defines the fourth member of the Shahai Formation, is characterized by high inertinite contents that range from 14 to 42.5 vol.%. The average content of inertinite in the early Albian is 24.6 vol.% and is higher than that of the other three units. Unit D, which developed during the middle and late Albian defines the Fuxin Formation, is characterized by inertinite contents that range from 8.7 to 17.4 vol.% and display a downward trend.

4.2 Inertinite reflectance

The characteristics of inertinite reflectance from all mudstone samples are summarized in Table 1. Units A, B and C are characterized by relatively high values of inertinite reflectance ranging from 1.0–4.3%Ro, 0.8–3.4%Ro, and 0.6–3.8%Ro, respectively. Unit D is characterized by inertinite reflectance values that range from 0.8% to 2.6%Ro and display a decreasing trend upwards. Unit A contains a high proportion (89%) of inertinite with reflectance values between 1.8 and 3.5%Ro. In Unit B, most (69%) inertinite contents have reflectance values between 1.8 and 3.5%Ro, while 31% of inertinite contents have low reflectance values less than 1.8%Ro. Unit C comprises a proportion (35.5%) of inertinite reflectance between 1.8% and 3.5%Ro and a relatively high proportion (64.3%) of inertinite reflectance less than 1.8%Ro. In Unit D, most (81%) inertinite contents have reflectance values less than 1.8%Ro.

4.3 PAHs compounds

A total number of 18 PAHs were detected from ten selected mudstone samples (Fig. 8 and Table 2). The major PAHs compounds identified in all samples are I-Naphthalene, II-Fluorene, III-Biphenyl, IV-Dibenzothiophene, V-Dibenzofuran, VI-Phenanthrene, VII-Anthracene, VIII-Retene, IX-Fluoranthene, X-Benzo(a)fluorine, XI-Benzo(b)fluorine, XII-Pyrene, XIII-Benz(a)anthracene, XIV-Chrysene, XV-Benzofluoranthenes, XVI-Benzo(e)pyrene, XVII-Benzo(a)pyrene, and XVIII-Perylene with more or less intense methyl derivatives of the respective compounds. Quantitative analyses of PAHs show that total concentrations vary from 0.081 to 3.846 μg/g mudstone with an average of 1.836 μg/g mudstone (Table 2). Vertically through the succession, the PAHs compounds of Unit C are higher than those of the other three

units. In ten mudstone samples (Table 2), the high-molecular-weight of PAHs (5-ring) are identified, such as XVI-Benzo(e)pyrene (0.0004–0.1598 μg/g mudstone), XVII-Benzo(a)pyrene (0.0004–0.3 μg/g mudstone), and XVIII-Perylene (0–0.1878 μg/g mudstone).

5. Discussion

5.1 Evidence of wildfire

Evidence of wildfire is provided by analysis of inertinite (charcoal) and PAHs through the studied section.

5.1.1 Organic petrographic evidence of wildfire

Charcoal, the byproduct of wildfires, provides valuable information on the historical occurrence of wildfires (Scott and Glasspool, 2006; Glasspool and Scott, 2010). Inertinite is widely recognized as a synonym for charcoal and is widely accepted as direct evidence of wildfires in geological deep time (Scott and Glasspool, 2007). Although inertinite may originate from multiple paths (e.g., wildfires and degradation of organic matter), observations on modern charcoal deposits and experimental charring studies indicate that inertinite is formed almost exclusively as a product of wildfires (Jones et al.,1991; Jones,1994; Scott and Glasspool, 2007).

Abundant charcoal particles from several microns to several centimeters were observed in hand specimens, in transmitted and reflected light microscopy and under the SEM (Figs. 4, 5, 6 and 7). These macroscopic and microscopic features are consistent with the characteristics of charcoal described by Scott (2010). In the study area, relative inertinite contents (8.3–42.5 vol.%) (Table 1) are very similar to relative inertinite values (mostly 10–45 vol.%) in coals from the Lower Cretaceous Erlian, Hailar, and Sanjiang basins in northeastern China (Wang et al., 2019b). Inertinite contents in Unit C are significantly higher than those in the other three units (Fig. 3). This observation provides evidence for an elevated wildfire activity during the early Albian interval. The vertical variation of inertinite abundances in this study (Fig. 3) indicates that wildfires were widespread and frequent in northeastern China during the Lower Cretaceous, which is consistent with the interpretation of Lower Cretaceous “high-fire” conditions especially during the early Albian (Bond and Scott 2010; Diessel, 2010; Brown et

al. 2012).

5.1.2 PAHs evidence of wildfire

PAHs are a class of compounds consisting of two or more benzene rings fused in a linear, angular, or clustered arrangement (Chefetz et al., 2000). PAHs originate from two main sources in sedimentary strata, including incomplete combustion of fossil fuels such as coal and petroleum, and other organic matter such as wood (Thompson et al., 2017), as well as degradation of organic matter by microorganisms during diagenesis (Zakir Hossain et al., 2013; Meng et al., 2019). PAHs from pyrogenic sources (combustion of organic matter) mainly consist of 3–6 ring PAHs, which are distinguished by high abundances of unsubstituted compounds (Page et al., 1999; Liu et al., 2005; Denis et al., 2012; Xu et al., 2020c). Unsubstituted PAHs have been extensively regarded as wildfire indicators in sedimentary rocks due to their pyrolytic origin (Liu et al., 2005; Grice et al., 2007; Marynowski and Simoneit, 2009; Zakir Hossain et al., 2013). However, the abundance of PAHs is likely to be affected by the thermal history of a basin, which should be seriously considered before interpreting the source of PAHs (Murchison and Raymond, 1989; Jiang et al., 1998; Zhang et al., 2020). Because of the influence of diabase intrusion on the sedimentary strata at the bottom of the Shahai Formation (Zhang et al., 2003; Zhu et al., 2007), the relatively high abundance of PAHs in units A and B might be considered to be the result of rapid heating of organic material by magmatic intrusions (Murchison and Raymond, 1989). In the study area, high-molecular-weight PAHs (3–5 ring) were identified, whereas the PAHs with 6-rings were not found. The occurrence of pyrogenic PAHs indicates that a wide range of wildfires occurred in the Fuxin Basin during the Lower Cretaceous, and the abundance of 3–5 ring PAHs indicates that wildfire activity in Unit C was more intense and frequent than for the other three units. Fluoranthene, pyrene, benz[a]anthracene, benzofluoranthenes, benzo[e]pyrene, benzo[a]pyrene, indeno[1,2,3-cd]pyrene, benzo[ghi]perylene and coronene are commonly considered to be primarily of combustion origin (Zakir Hossain et al., 2013). The higher the number of aromatic rings, the stronger the antioxidant ability of PAHs (Xu et al., 2020c). Studies show that benzo[e]pyrene is highly resistant to oxidation processes (Marynowski et al., 2011) and is the most stable PAH among the 5-ring PAHs (Jiang et al., 1998; Sullivan et al.,

1989). The occurrence of PAHs with 5-rings in this study (Fig. 8) also indicates that a wide range of wildfires occurred in the Lower Cretaceous Fuxin Basin. PAH compounds show the different aromatic rings at different combustion temperatures (Zakir Hossain et al., 2013). The high abundances of high-molecular-weight PAHs represent a relatively high combustion temperature, which can provide information on wildfire intensity (Finkelstein et al., 2005; Denis et al., 2012; Zakir Hossain et al., 2013). In the study area, the relatively high abundance of PAHs with 5-rings (benzo[e]pyrene, benzo[a]pyrene and perylene) in Unit C during the early Albian mostly shows high wildfire intensity.

5.2 Wildfire types inferred from inertinite reflectance

Inertinites from wildfire activity show a range of reflectance values which are directly related to fire type and temperature (Scott and Jones, 1994; Jasper et al., 2016). Experimental data have demonstrated that high reflectance of inertinite may be the result of increasing temperature during wildfire activity (Jones et al.,1991; Scott and Glasspool, 2007). Although there is no absolute linear relationship between inertinite reflectance and burning temperature, a correlation has been expressed by a linear regression equation derived by Jones (1997): $T = 184.10 + 117.76 \times \%Ro$ ($r^2 = 0.91$). Where T is the burning temperature and %Ro is the measured inertinite reflectance.

Based on experimental data, the ranges of inertinite reflectance for units A, B, C and D are 1.0–4.3%Ro, 0.8–3.4%Ro, 0.6–3.8%Ro and 0.8–2.6%Ro, respectively. According to the above equation, the corresponding temperature ranges of inertinite formation are 303.4–696.2 °C, 275–589.7 °C, 255–626.8 °C and 278.7–485.7 °C, respectively. Wildfires can be grouped into three types by different burning temperatures, namely, ground fire, surface fire and crown fire (Scott and Jones, 1994; Petersen and Lindström, 2012; Wang et al., 2019b). Ground fires that burn organic material below the litter, generally produce maximum temperatures around 400 ºC, while surface fires that burn litter and herbaceous and shrubby plants, can reach temperatures around 600 °C. Crown fires typically burn canopies of trees and larger shrubs, which can produce intense heat with temperatures of 800 °C or higher (Scott and Jones, 1994; Petersen and Lindström, 2012; Wang et al., 2019b). In the study area, mudstone samples in units A and B have seemingly circumvented the normal thermal history, with the increase of

inertinite reflectance being caused by rapid heating in an environment of magmatic intrusive activity (Murchison and Raymond, 1989). Therefore, units A and B we abandoned for analysis of inertinite reflectance, burning temperature and wildfire type. Although the range of the inertinite reflectance values in Unit C is wide, inertinite with low reflectance values between 0.6 and 1.8%Ro accounts for 64.3% of the inertinite content of Unit C. These inertinites have low burning temperatures between 255 and 400 °C, indicating that they are predominantly derived from ground fires (Petersen and Lindström, 2012; Fig. 10). In addition, inertinite with reflectance values between 1.8 and 3.5%Ro accounts for 35.5% of the total inertinite population in Unit C. Their formation temperatures are between 400 and 600 °C, inferring relatively high temperature surface fires (Petersen and Lindström, 2012; Fig. 10). According to Jones (1996) and Scott (2010), the cell walls of inertinite become homogenized above a temperature of 300–325 °C. In Unit C, the inertinite observed under SEM shows homogenized cell walls (Fig. 7), indicating that the burning temperature of wildfire was higher than 300–325 °C. In Unit D, the proportion of inertinite with reflectance values less than 1.8%Ro increases to 81%, while inertinite with reflectance values between 1.8 and 3.5%Ro accounts for 19% of the inertinite population of Unit D. These results indicate a decrease in burning temperatures though time in Unit D.

5.3 Atmospheric oxygen levels estimated from inertinite contents

Atmospheric oxygen concentration (pO_2) varied dramatically during the Mesozoic (Belcher and McElwain, 2008; Belcher et al., 2010; Mills et al., 2016). Based on models, elevated pO_2 levels have been proposed globally during the Albian (Bergman, 2004; Glasspool and Scott, 2010; Wang et al., 2019b) with a maximum value up to 29% (Glasspool and Scott, 2010), significantly higher than present-day 21% concentration (Belcher and McElwain, 2008; Belcher et al., 2010). Berner (2009) predicted pO_2 levels below present-day values until the Albian, thereafter, rising above 21%. Oxygen plays an important role in the occurrence of wildfires and the formation of inertinite (Scott, 2010; Shao et al., 2012; Glasspool et al., 2015; Yan et al., 2019). Experimental data reveal that fire activity would be entirely switched off below pO_2 levels of 16%, greatly suppressed below pO_2 levels of 18.5%, and rapidly enhanced between pO_2 levels of 19–22% (Belcher et al., 2010). If pO_2 significantly exceeded 25%, fire

frequencies would have been widespread and even globally in aerial extent (Wildman et al., 2004; Belcher et al., 2010). Previous studies considered that inertinite contents in the sedimentary record could be used to infer atmospheric pO_2 levels (e.g., Scott and Glasspool, 2007; Glasspool and Scott, 2010).

Glasspool and Scott (2010) and Glasspool et al. (2015) compiled a large database on inertinite contents of coals from different geological periods, and then proposed an inertinite to pO_2 calibration curve. Although this model is based on inertinites found in coals, the relative proportion of the inertinite in the kerogens contained in the mudstones may also give an approximation on the atmospheric oxygen level (Liu et al., 2020). In this study, the relative inertinite contents with an average of 24.6 vol.% from all mudstone samples in Unit C would indicate a pO_2 level of ~25% during the early Albian based on the model of Glasspool et al. (2015) (Fig. 11). The relative content of inertinites in contemporaneous coals of the Fuxin Basin ranged from 12% to 19% (Yang, 1996), and these inertinite contents would give a pO_2 level between approximately 23% to 24%. In addition, the pO_2 level estimated from the inertinite contents in the Albian coals of other regions in NE China is around 25.3% (Wang et al., 2019b). The results from coals and mudstones are very similar, and are in accordance with the models of Bergman et al. (2004), Arvidson et al. (2006) and Glasspool and Scott (2010) that estimated pO_2 levels in the early Albian atmosphere were around 25%. As a result, pO_2 level may be calculated from relative inertinite contents in mudstone, nevertheless, it needs to be used with caution. From this it can be interpreted that pO_2 levels during the early Albian were much higher than the minimum needed for sustained combustion, and even reached a situation where fires become common. The high pO_2 levels would have led to greatly increased plant flammability, which is consistent with a global record of widespread wildfires during the Lower Cretaceous (Belcher et al., 2010; Diessel, 2010; Wang et al., 2021a; Wang et al., 2019b, 2020b).

5.4 Wildfires linked to the evolution of early angiosperms

A growing body of fossil evidence documents angiosperms first evolved in the Lower Cretaceous and subsequently underwent a rapid radiation to gain ecological dominance by the Upper Cretaceous (e.g., Bond and Scott, 2010; Friis et al., 2010; Brown et al., 2012; Coiro et

al. 2019). The oldest recognized angiosperms from the megafossil record come from the Barremian aged Yixian Formation (Friis et al., 2010) from the North China Plate. However, while the megafossil record of Cretaceous angiosperms is often scant, records of their distinctive pollen demonstrate that the group first appeared in the Barremian at low paleolatitudes and diversified and spread into higher northern and southern paleolatitudes (Couper, 1958; Coiro et al., 2019). The earliest angiosperms appeared in the middle paleolatitudes during the Albian noted by the presence of pollen genera including *Cupuliferoidaepollenites*, *Fraxinoipollenites*, *Phimopollenites*, *Rousea* and *Tricolpites* (Korasidis et al., 2016), and reached high-latitude Arctic area during the Cenomanian including the pollen genera *Tricolpites* sp. and *Retitricolpites* sp. (Brenner, 1976; Galloway et al., 2012; Coiro et al. 2019).

In the North China Plate, Lower Cretaceous continental strata are widely-developed and contain abundant palynomorphs and excellently preserved angiosperm macrofossils which have been used for biostratigraphy and to explore early angiosperm evolution. Lower Cretaceous angiosperm pollen from the North China Plate has been subdivided into five distinct stages from the Barremian, Aptian, early and middle Albian, late Albian, and latest Albian–Cenomanian (Song, 1986). In the Barremian, the monosulcate angiosperm pollen *Clavatipollenites* began to appear in low numbers. During the Aptian, tricolpate angiosperm pollen appeared alongside *Clavatipollenites* but was relatively monotonous morphologically, with angiosperm pollen comprising approximately 5% of Aptian palynofloral assemblage (Song, 1986). In the early and middle Albian, tricolpate pollen types diversified markedly and included more complex forms, and the proportion of angiosperm pollen rose to approximately 10%. In the late Albian, tricolporate angiosperm pollen first appeared, with the proportion of the angiosperm pollen in palynofloras remaining at approximately 10%. The latest Albian–Cenomanian palynofloras are marked by the first appearance of oblate tricolporate and triporate angiosperm pollens and the proportion of angiosperm pollen in palynofloras at this time exceeding 10% (Song, 1986). These five floral stages clearly show the diversification and rise in abundance of angiosperm pollen through the North China Plate during the Lower Cretaceous.

Looking more locally at the study area in western Liaoning Province, the Lower

Cretaceous has previously been divided into the Jibei, Jehol and Liaoxi regional stratigraphic stages (Wan et al., 2013; Fig. 2). Of these the Barremian–lower Aptian aged Jehol stage corresponds to the Yixian and Jiufotang formations and includes the stratigraphically oldest angiosperm megafossils (Friis et al., 2010) including *Archaefructus sinensis* and *Sinocarpus decussatus* (Sun et al., 1998, 2002; Leng and Friis, 2003; Zhou et al., 2003; Hilton and Bateman, 2006). The upper Aptian-Albian aged Liaoxi regional stage corresponds to the Shahai, Fuxin and Sunjiawan formations in ascending order (Fig. 2). The Shahai and Fuxin formations contain the Fuxin flora that is dominated by ferns, Ginkgoales and conifers with abundant cycads and Equisetales and occasional angiosperms (Deng et al., 2012; Wan et al., 2013). However, despite the megaflora of the Shahai and Fuxin formations being similar, the *Cicatricosisporites-Pinuspollenites-Classopollis* palynological assemblage in the Shahai Formation contains typical tricolpate angiosperm pollen including *Tricolpites* and *Tricolpopollenites* (Tao et al., 2013), while angiosperm pollen is abundant in the *Cicatricosisporites-Laevigatosporites-Piceaepollenites* palynological assemblage in the lower part of the Fuxin Formation (Tao et al., 2013). Angiosperms with complex reticulate leaf venation including *Asiatifolium elegans*, *Chengzihella obovata*, *Jixia pinnatipartita*, *Shenkuoia claoneura* and *Rogersia lanceolate* (Sun et al., 1992) occur in the *Ruffordia goepperti-Dryopterites* assemblage from the lower-middle part of the Fuxin Formation (Deng et al. 2012). The upper part of the Fuxin Formation contains the *Ctenis lyrata-Chilinia* assemblage (Chen et al. 1988) in which angiosperms are relatively abundant and include *Populus* sp., *Vitiphyllum* sp. and *Trochodendroides* sp. (Deng et al. 2012). Finally, in the Sunjiawan Formation angiosperm pollen became a very common component *Appendicisporites-Laevigatosporites* assemblage (Tao et al., 2013). To summarize, the abundance and diversity of angiosperms show a distinct increase from the Yixian Formation to the Sunjiawan Formation during the early Cretaceous in the western Liaoning region.

Wildfires have existed as a significant evolutionary force that may have affected the nature of the vegetation itself (Bond and Keeley, 2005; Brown et al., 2012). Many plants have acquired adaptive traits that enable them to cope with fire and reproduce in fire-prone ecosystems (Bond and Scott, 2010; Brown et al., 2012; Belcher et al., 2021). Furthermore, previous studies have suggested that the spread and diversification of angiosperms in the

Cretaceous was facilitated by fire regimes (e.g., Bond and Scott, 2010; Friis et al., 2010; Brown et al., 2012). It is especially noteworthy that the earliest known fossil flowers are preserved as charcoalified mesofossils (e.g., Friis et al., 2010), further emphasizing the relationship of angiosperms with fire. The earliest angiosperms were weedy plants characterized by small herbaceous or shrubby habits with little wood that formed the understory and ground cover (Friis et al., 2010; Royer et al., 2010; Brown et al., 2012). Brown et al. (2012) proposed that herbaceous plants may allow surface fires to burn rapidly. In the study area, 35.5% of inertinite content of the early Albian have experienced relatively high burning temperature between 400 and 600 °C, indicating that they are mainly derived from surface fires. This type of wildfire may have had little effect on soils such that plant roots and seed banks may not have been killed, allowing for rapid regrowth of vegetation and especially herbaceous and shrubby plants following rainfall (Brown et al., 2012). Highly productive weedy angiosperms favour rapid fuel accumulation, which may promote shorter fire cycles under suitable physical preconditions (Bond and Scott, 2010). Frequent Cretaceous wildfires could open up adjacent closed environments and create open sunlit habitats favorable to the expansion of early angiosperms (e.g., Berendse and Scheffer, 2009; Bond and Scott, 2010; Belcher et al., 2021).

In the Lower Cretaceous of northeast China, the Fuxin flora from the Shahai and Fuxin formations provided an appropriate source of fuel for wildfires. The spores and pollen grains (Fig. 4e-j) and plant fossil fragments (Fig. 5k and 5l) observed in the early Albian Fuxin Basin also provide evidence for the existence of ferns, conifers and cycads characteristic of the Fuxin Flora. Angiosperms played an increasingly important role in Lower Cretaceous floras in NE China from the Barremian onwards increasing in abundance and diversity through time. The widespread wildfires in the Fuxin Basin during the early Albian support the opinion that wildfires may have played an important role in promoting the spread and diversification of early angiosperms in this region. In particular, we infer that frequent surface fires were conducive to the rapid recovery of the early low-stature angiosperms after burns during the early Albian.

Huang et al. (2007) proposed that atmospheric CO_2 fertilization increases photosynthetic rates and rising pCO_2 has a positive effect on plant growth due to increasing availability of

carbon. Moreover, enhanced leaf vein densities in the evolution of early angiosperms also potentially increased maximum photosynthetic rates (Brodribb and Field, 2010). Elevated pCO_2 levels in the early Albian (Haworth et al., 2005; Hong and Lee, 2012; Sun et al. 2016; Barral et al., 2017; Xu et al., 2022) and high leaf vein densities during the Lower Cretaceous (Field et al., 2011) would have led to an increase in primary productivity, and consequently, greater fuel loads (He et al., 2018). Rapid accumulation of vegetation with high productivity and rapid recovery in the Lower Cretaceous would have provided sufficient fuel for the frequent occurrence of wildfires under high pO_2 levels, and further promoted the spread of early angiosperms.

5.5 Continental wildfires linked to the early Albian OAE 1b

OAE 1b is characterized by several short-term perturbations of the global carbon cycle and multiple black mudstone horizons with relatively enhanced organic carbon contents (Trabucho Alexandre et al., 2011). Stratigraphically, OAE 1b spans the late Aptian to early Albian (~110.5–114.5 Ma) and each perturbation corresponds to one of the four sub-events comprising the uppermost Aptian Jacob sub-event, and the lower Albian Kilian, Paquier and Leenhardt sub-events (Coccioni et al., 2014; Li et al., 2016; Matsumoto et al. 2020).

5.5.1 Recognition of the Jacob sub-event

The Jacob sub-event is the first organic-rich expression during OAE 1b (Coccioni et al., 2014; Matsumoto et al. 2020). In western Tethys, the Jacob sub-event is ~75 cm thick with a TOC content up to 2.5–8% (Herrle 2002; Heimhofer et al. 2006; Coccioni et al., 2014; Sabatino et al., 2015; Matsumoto et al. 2020). The Jacob sub-event is characterized by a weak negative carbon isotope shift within the second late Aptian positive carbon isotope excursion (Coccioni et al., 2014; Herrle et al., 2015). Matsumoto et al. (2020) conducted a comparative analysis of the negative $\delta^{13}C_{carb}$ excursion of the Jacob sub-event in western Tethys and the Pacific Ocean, indicating that it is marked by a weak negative $\delta^{13}C_{carb}$ shift of ~0.7‰ in western Tethys (Coccioni et al., 2014; Fig. 9).

In the study area, the Aptian/Albian boundary was placed at the boundary between Unit B and Unit C corresponding with an age greater than 112.6 ± 1.7 Ma according to zircon U-Pb

dating analyses (Fig. 9; Xu et al., 2022), constraining Unit B to the latest Aptian approximately. In the latest Aptian Fuxin Basin, a weak negative $\delta^{13}C_{org}$ excursion of -22.7‰ occurred in an interval of a positive $\delta^{13}C_{org}$ excursion near the Aptian/Albian boundary. The peak value of the negative $\delta^{13}C_{org}$ shift corresponds to a relatively high TOC value up to 1.1%. From this we interpret that the slight negative $\delta^{13}C_{org}$ excursion below the Aptian/Albian boundary may represent the Jacob sub-event (Fig. 9).

5.5.2 Recognition of the Kilian sub-event

The Kilian sub-event is the organic-rich expression of the second sub-event of OAE 1b (Coccioni et al., 2014). Most studied successions in western Tethys and eastern North Atlantic show that the thickness of the Kilian sub-event varies between ~38 cm and 80 cm with TOC contents ranging of ~1—~5% (e.g., Herrle, 2002; Herrle et al., 2004; Friedrich et al., 2005; Trabucho Alexandre et al., 2011; Coccioni et al., 2014; Sabatino et al., 2015). The Kilian sub-event also exhibits a short-term negative carbon isotope excursion above the high carbon isotope records of the Jacob sub-event (Herrle et al., 2004; Coccioni et al., 2014). In the western Tethys and the eastern Pacific, the Kilian sub-event is characterized by a negative $\delta^{13}C_{carb}$ excursion reaching ~1‰ (Sabatino et al., 2015; Matsumoto et al. 2020) and a large negative $\delta^{13}C_{org}$ excursion reaching -26.3‰–-25.8‰ (Navarro-Ramirez et al., 2015; Sabatino et al., 2015). In the eastern North Atlantic (DSDP Site 545, Mazagan Plateau), the Kilian sub-event shows a distinct negative carbon isotope excursion ranging from ~2‰ prior to the organic-rich interval to an average value of 0.75‰ during the sub-event, and then a gradual return to carbon isotopic values of ~1.2‰ at its termination (e.g., Herrle, 2002; Herrle et al., 2004; Friedrich et al., 2005; Trabucho Alexandre et al., 2011). In terrestrial records close to the western Pacific in southeastern China, the Kilian sub-event is expressed as a negative excursion with an average $\delta^{13}C_{org}$ value of -26.1‰ occurring the 44.4–44.7 m interval in the Shipu section and an average $\delta^{13}C_{org}$ value of -27.0‰ in the Chong'an section (Hu et al., 2014).

In the early Albian Fuxin Basin, from the bottom to the top the first interval of negative $\delta^{13}C_{org}$ excursion decreases from -26.1‰ to -27‰, and then back to -25.6‰ (Fig. 9). Amongst these, the peak value of the negative excursion corresponds with high TOC values up to 4.76% (Xu et al., 2022). Carbon isotopic records during the early Albian are the first distinctly

570 negative δ13Corg excursion above the top of the positive δ13Corg excursion, which coincides
571 with the characteristics of the Kilian sub-event, a short negative excursion above the positive
572 excursion in the carbon isotope record of the Jacob sub-event (Herrle et al., 2004). In addition,
573 the age of the first negative excursion interval is younger than 112.6 ± 1.7 Ma according to the
574 zircon U-Pb dating analysis (Xu et al., 2022), which could be regarded as the Kilian sub-event
575 equivalent.
576
577 5.5.3 Recognition of the Paquier sub-event
578 The Paquier sub-event is the organic-rich expression of the third sub-event of OAE 1b
579 (Coccioni et al., 2014). In western Tethys and western North Atlantic, the Paquier sub-event is
580 0.25–1.63 m thick and has TOC contents up to 8–12.3% (e.g., Herrle, 2002; Huber et al. 2011;
581 Coccioni et al., 2014; Sabatino et al., 2015; Matsumoto et al. 2020). The Paquier sub-event is
582 defined by a negative excursion in both marine carbonate and organic matter carbon isotope
583 records (e.g., Erbacher et al., 2001; Herrle et al., 2004; Tsikos et al., 2004). In Tethys and the
584 eastern Pacific, the Paquier sub-event commences with an abrupt negative $\delta^{13}C_{carb}$ shift
585 reaching values as low as -0.68–~2.2‰, whereas $\delta^{13}C_{org}$ values exhibit a gradual negative shift
586 reaching -27‰ (e.g., Coccioni et al., 2014; Sabatino et al., 2015; Navarro-Ramirez et al., 2015;
587 Li et al., 2016). In terrestrial records of the western Pacific in southeastern China, the Paquier
588 sub-event displays the strongest negative excursion with a $\delta^{13}C_{org}$ peak value of -27.8‰ in the
589 Shipu section, and an average $\delta^{13}C_{org}$ value of -27.9‰ in the Chong'an section (Hu et al.,
590 2014). In terrestrial settings close to eastern Tethys in northwestern China, the Paquier event
591 occurs from 142.2 m–166.8 m in the Hanxiagou section from the Jiuquan Basin and exhibits a
592 strong negative $\delta^{13}C_{org}$ excursion from -27‰ to -21.7‰ representing an ~5‰ change (Zhao et
593 al., 2022).
594 In the study area, the second interval of negative $\delta^{13}C_{org}$ shift from the bottom of the early
595 Albian decreases from -24.8‰ to -26.2‰, followed by a positive $\delta^{13}C_{org}$ excursion with $\delta^{13}C_{org}$
596 values up to -24.9‰ (Fig. 9; Xu et al., 2022). The magnitude of the negative excursion (1.4‰)
597 in the present study closely matches those in terrestrial records (~1.5‰) from the Paquier sub-
598 event, including evidence from fossil wood in Japan (Ando et al., 2007), palustrine nodules
599 from the USA (Ludvigson et al., 2010), and terrestrial organic matter from southeastern China

(Hu et al., 2014). High resolution carbon isotope records from the Vocontian Basin show that the Paquier sub-event follows after the Kilian sub-event and has a carbon isotope record comprising a short negative excursion after a brief recovery above the Kilian sub-event (Fig. 9; Herrle et al., 2004). A similar negative $\delta^{13}C_{org}$ excursion in the early Albian Fuxin Basin suggests that it represents the counterpart of the Paquier sub-event.

5.5.4 Recognition of the Leenhardt sub-event

The Leenhardt sub-event is the organic-rich expression of the fourth sub-event of OAE 1b and has been documented in many regions of the world (Coccioni et al., 2014; Navarro-Ramirez et al., 2015; Li et al., 2016). In western Tethys, the Leenhardt sub-event is 29 cm–~92 cm thick with TOC contents of 0.95–3% (Herrle, 2002; Coccioni et al., 2014; Sabatino et al., 2015). In Tethys and the eastern Pacific, the Leenhardt sub-event is characterized by a negative $\delta^{13}C_{carb}$ excursion reaching -0.1‰–~1‰ with negative $\delta^{13}C_{org}$ excursion values as low as -28‰ (Coccioni et al., 2014; Navarro-Ramirez et al., 2015; Li et al., 2016). In terrestrial records close to the western Pacific in southeastern China, the Leenhardt sub-event shows a relatively weak negative $\delta^{13}C_{org}$ excursion with an average $\delta^{13}C_{org}$ value of -27.6‰ in the Chong'an section (Hu et al., 2014). In terrestrial records near eastern Tethys from northwestern China, $\delta^{13}C_{org}$ values decrease from -26.1‰ to -22.8‰ in the 228.3 m–236.3 m interval of the Hanxiagou section in the Jiuquan Basin (Zhao et al., 2022).

In the early Albian Fuxin Basin, from the bottom to the top, the third interval of negative $\delta^{13}C_{org}$ excursion decreases from -25.7‰ to -26.6‰, and then returns back to -25.1‰ at its termination (Xu et al., 2022). The magnitude of the negative excursion (1.5‰) is similar to those in the eastern Pacific Andean Basin (Navarro-Ramirez et al., 2015) and the western North Atlantic (ODP site 1049 off northern Florida, Blake Nose escarpment; Huber et al., 2011), but is higher than those of hemipelagic and platform carbonates in Tethys, such as from the Umbria-Marche Basin (Coccioni et al., 2014) and the Bangbu section in southern Tibet, China (Li et al., 2016). The negative $\delta^{13}C_{org}$ excursion with a peak value up to -26.6‰ is comparable to that of terrestrial records close to the western Pacific from southeastern China (Hu et al., 2014) and that of organic matter in the eastern Pacific Andean Basin (Navarro-Ramirez et al., 2015). Therefore, we conclude that this negative $\delta^{13}C_{org}$ shift from the early Albian Fuxin Basin

most likely represents the Leenhardt sub-event.

In the study area, four sharp, short-term negative $\delta^{13}C_{org}$ excursion occur during the late Aptian to early Albian and each corresponds with relatively high TOC values. Furthermore, these correlate well stratigraphically with the Jacob, Kilian, Paquier and Leenhardt sub-events of OAE 1b on the basis of zircon U-Pb age and changing trends and magnitudes of carbon isotope excursions. Based on carbon isotope chemostratigraphy, the sub-events of OAE 1b in the Fuxin Basin can therefore be correlated with six representative research cases including western Tethys, eastern Pacific, western North Atlantic and China (Fig. 9). This comparative analysis indicates that OAE 1b has a global signature and is not only expressed in marine settings but also can be recognized from the terrestrial record.

In the Fuxin Basin, mudstone samples in units A and B have seemingly circumvented the normal thermal history, because of the influence of diabase intrusion on the sedimentary strata at the bottom of the Shahai Formation (Zhang et al., 2003; Zhu et al., 2007). Therefore, we abandoned the analysis of wildfire events in units A and B. Three short-term increases of inertinite content and inertinite reflectance correspond to three negative $\delta^{13}C_{org}$ excursions and relatively high TOC values during the early Albian interval (Fig. 10). In the study area, the resulting estimates of inertinite content and inertinite reflectance provide evidence for enhanced continental wildfires during the Kilian, Paquier and Leenhardt sub-events of the OAE 1b (Fig. 10).

The widespread occurrences of wildfires depend on a combination of factors, such as flammable fuel accumulation, atmospheric pO_2 level, moisture content and ignition mechanism (Bond et al. 2010; Glasspool et al., 2015). The lush Fuxin flora in western Liaoning region during the late Albian–Aptian interval (Deng et al. 2012), would have provided an appropriate source of fuel. The relatively humid palaeoclimate in the early Albian (Xu et al., 2020a) would have reduced the likelihood of wildfire. However, the high pO_2 level of ~25% estimated in the early Albian might render vegetation with relatively high moisture more susceptible to combustion (Glasspool et al., 2015). Five potential sources (apart from human activity) of triggering ignition include lightning strikes, volcanic eruptions, meteor strikes, sparks from rock falls and spontaneous combustion (Belcher et al., 2010; Glasspool et al., 2015). Abundant local volcanic eruptions occurred in the western Liaoning region during the Lower Cretaceous

(Cai et al., 2010), which may have acted as the main source of ignition for wildfires.

Continental wildfires destroy land surface vegetation systems and soil structure, which increase soil erosion by continental chemical weathering and transfer of land materials (e.g., minerals, plant residues, charcoal and nutrient elements) into lacustrine and marine environments (Algeo and Ingall, 2007; Brown et al. 2012; Glasspool et al., 2015) contributing to eutrophication and anoxia in lacustrine and in contemporaneous oceanic systems (Brown et al. 2012; Yan et al., 2019; Xu et al., 2020a, 2022). In the study area, the high inertinite contents show that wildfires prevailed in northeastern China during the Lower Cretaceous. In addition, the vertical variation patterns of inertinite content and inertinite reflectance indicate short-term increasing trends of wildfire activity during the Kilian, Paquier and Leenhardt sub-events of the Albian OAE 1b (Fig. 10). Chemical weathering indices have been used to quantitatively track secular variation in chemical weathering intensity, with implications for palaeoclimate reconstruction (Nesbitt and Young, 1982; Fedo et al., 1995; Xu et al., 2018; Lu et al., 2020; Xu et al., 2020a; Gao et al., 2021). Various chemical weathering indices were compiled to illuminate the chemical weathering trend in the Fuxin Basin during the Lower Cretaceous, including the Chemical Index of Alteration (CIA; Nesbitt and Young, 1982), Mafic Index of Alteration for Oxidative weathering environments ($MIA_{(O)}$; Babechuk et al., 2014) and Weathering Index of Parker (WIP; Parker, 1970). The degree of chemical weathering calculated using the chemical weathering indices (CIA, WIP and $MIA_{(O)}$) show an increasing trend during the early Albian OAE 1b interval (Xu et al., 2020a). In the study area, sandstones associated with abundant charcoal fragments have been identified in the Fuxin Basin (Fig. 5a and 5c), which probably represents a post-fire erosion deposit. These sandstones contain charcoals and may be related to increased soil erosion after wildfires. As the result of frequent wildfire activity and intensified chemical weathering, abundant nutrients and organic matter may be transported from continents into lakes where nutrients might increase productivity in surface waters. Transported tree trunk fossils were identified in lacustrine environments of the early Albian (Fig. 5b, 5g and 5h) providing evidence that terrestrial plants were flushed into lakes. Many fossil charcoals identified in lacustrine mudstone in the DY-1 borehole (Fig. 5d, 5e and 5f) may also demonstrate that high flux of nutrients and organic matter produced by increasing wildfire activity and chemical weathering were flushed into lakes through surface

runoff. Ultimately, decaying organic matter in surface waters, including terrestrial plants and lacustrine plankton, consumed oxygen during downward passage through the water column, which in turn led to anoxia in lakes (Fig. 12). This unit correlates with the early Albian OAE 1b, inferring that frequent wildfire activity at this time promoted high nutrient levels and organic matter that were flushed into marine systems, triggering contemporaneous ocean anoxic event. In this context, many organisms gradually died and organic matter was buried and preserved with an expansion of the oxygen-minimum zone. These results support previous work which proposed that increased wildfires activity stimulated eutrophication and anoxia in lakes and oceans and ultimately organic carbon burial (Brown et al., 2012; Yan et al., 2019; Boudinot and Sepúlveda, 2020).

6. Conclusions

(1) High levels of inertinite contents and PAHs in mudstone samples provide evidence for widespread wildfires during the early Albian. The main types of wildfires in the early Albian were ground and surface fires, and the frequency of surface fires was high. Inferred pO_2 levels in the early Albian atmosphere, as estimated from inertinite contents, were ~25%, which is much higher than the minimum needed for sustained combustion.

(2) Wildfire activity in the Fuxin Basin was a pivotal evolutionary force shaping vegetation diversification during the early Albian. Sufficient fuel accumulation and frequent surface fires under high pO_2 levels had a dramatic effect on the evolution of early angiosperms in Lower Cretaceous landscapes.

(3) Wildfires destroyed vegetation cover and soil structure in the Fuxin Basin during the early Albian, which enhanced post-fire erosion under the conditions of intensified continental weathering. Post-fire erosion and vegetation destruction may have promoted elevated levels of nutrients and organic matter that were flushed into lakes and thereby contributed to eutrophication and anoxia in lacustrine and contemporaneous oceanic systems. These corresponds to the Kilian, Paquier and Leenhardt sub-events of the early Albian OAE 1b and suggest a temporal linkage between terrestrial and marine environmental perturbations.

Declaration of Competing Interest

The authors declare that they have no known competing financial interests or personal relationships that could have appeared to influence the work reported in this paper.

Acknowledgments

This study was supported by the Yue Qi Scholar Project of China University of Mining and Technology (Beijing), the National Natural Science Foundation of China (41572090; 42002128) and Shandong Key Laboratory of Depositional Mineralization & Sedimentary Mineral, Shandong University of Science and Technology (DMSM20190015). We thank the two anonymous reviewers for the insightful and helpful reviews.

References

Algeo, T.J., Ingall, E., 2007. Sedimentary C_{org}: P ratios, paleocean ventilation, and Phanerozoic atmospheric pO_2. Palaeogeogr. Palaeoclimatol. Palaeoecol. 256 (3–4), 130–155. https://doi.org/10.1016/j.palaeo.2007.02.029.

Ando, A., Kakegawa, T., 2007. Carbon isotope records of terrestrial organic matter and occurrence of planktonic foraminifera from the Albian stage of Hokkaido, Japan: ocean-atmosphere δ13C trends and chronostratigraphic implications. Palaios 22, 417–432. http://dx.doi.org/10.2110/palo.2005.p05-104r.

Arvidson, R.S., Mackenzie, F.T., Guidry, M., 2006. MAGic: A Phanerozoic model for the geochemical cycling of major rock-forming components. Am. J. Sci. 306(3), 135–190. https://doi.org/10.2475/ajs.306.3.135.

Babechuk, M.G., Widdowson, M., Kamber, B.S. 2014. Quantifying chemical weathering intensity and trace element release from two contrasting basalt profiles, Deccan Traps, India. Chem. Geol. 363, 56–75. https://doi.org/10.1016/j.chemgeo.2013.10.027.

Baker, S.J., Hesselbo, S.P., Lenton, T.M., Duarte, L.V., Belcher, C.M., 2017. Charcoal evidence that rising atmospheric oxygen terminated Early Jurassic ocean anoxia. Nat. Commun. 8, 15018. https://doi.org/10.1038/ncomms15018.

Barral, A., Gomez, B., Fourel, F., Daviero-Gomez, V., Lécuyer, C., 2017. CO_2 and temperature decoupling at the million-year scale during the Cretaceous Greenhouse. Sci. Rep. 7, 8310.

https://doi.org/10.1038/s41598-017-08234-0.

Belcher, C.M., McElwain, J.C., 2008. Limits for combustion in low O_2 redefine paleoatmospheric predictions for the Mesozoic. Science 321(5893), 1197-200. https://doi.org/10.1126/science.1160978.

Belcher, C.M., Hudspith, V.A., 2017. Changes to Cretaceous surface fire behaviour influenced the spread of the early angiosperms. New Phytol. 213, 1521–1532. https://doi.org/10.1111/nph.14264.

Belcher, C.M., Mills, B.J.W., Vitali1, R., Baker1, S.J., Lenton, T.M., Watson, A.J., 2021. The rise of angiosperms strengthened fire feedbacks and improved the regulation of atmospheric oxygen. Nat. Commun. 12, 503. https://doi.org/10.1038/s41467-020-20772-2.

Belcher, C.M., Yearsley, J.M., Hadden, R.M., McElwain, J.C., Rein, G., 2010. Baseline intrinsic flammability of Earth's ecosystems estimated from paleoatmospheric oxygen over the past 350 million years. PNAS 107(52), 22448–22453. https://doi.org/10.1073/pnas.1011974107.

Berendse, F., Scheffer, M., 2009. The angiosperm radiation revisited, an ecological explanation for Darwin's 'abominable mystery'. Ecol. Lett. 12, 865–872. https://doi.org/10.1111/j.1461-0248.2009.01342.x.

Bergman, N.M., 2004. COPSE: A new model of biogeochemical cycling over Phanerozoic time. Am. J. Sci. 304(5), 397–437. https://doi.org/10.2475/ajs.304.5.397.

Berner, R.A., 2009. Phanerozoic atmospheric oxygen: New results using the GEOCARBSULF model. Am. J. Sci. 309(7), 603–606. https://doi.org/10.2475/07.2009.03.

Boudinot, F.G., Sepúlveda, J., 2020. Marine organic carbon burial increased forest fire frequency during Oceanic Anoxic Event 2. Nat. Geosci. 13, 693–698. https://doi.org/10.1038/s41561-020-0633-y.

Bond, W.J., Keeley, J.E., 2005. Fire as a global 'herbivore': the ecology and evolution of flammable ecosystems. Trends Ecol. Evol. 20(7), 387–394. https://doi.org/10.1016/j.tree.2005.04.025.

Bond, W.J., Scott, A.C., 2010. Fire and the spread of flowering plants in the Cretaceous. New Phytol. 188, 1137–1150. https://doi.org/10.1111/j.1469-8137.2010.03418.x.

779 Brenner, G.J., 1976. Middle Cretaceous floral provinces and early migrations of angiosperms.
780 In: Beck, C.B. (Ed.), Origin and Early Evolution of Angiosperms. Columbia University
781 Press, New York, USA, pp. 23–47.
782 Brodribb, T.J., Feild, T.S., 2010. Leaf hydraulic evolution led a surge in leaf photosynthetic
783 capacity during early angiosperm diversification. Ecol. Lett. 13, 175–183.
784 https://doi.org/10.1111/j.1461-0248.2009.01410.x.
785 Brown, S.A.E., Scott, A.C., Glasspool, I.J., Collinson, M.E., 2012. Cretaceous wildfires and
786 their impact on the Earth system. Cretaceous Res. 36, 162–190.
787 https://doi.org/10.1016/j.cretres.2012.02.008.
788 Bustin, R.M., Guo, Y., 1999. Abrupt changes (jumps) in reflectance values and chemical
789 compositions of artificial charcoals and inertinite in coals. Int. J. Coal Geol. 38, 237–260.
790 https://doi.org/10.1016/S0166-5162(98)00025-1.
791 Cai, H.A., Li, B.F., Shao, L.Y., Xu, D.B., Shao, K., Zhou, Y.Y., 2011. Sedimentary
792 environments and coal accumulation patterns of the Lower Cretaceous Shahai Formation
793 in Fuxin Basin, Liaoning Province. J. Palaeogeogr. 13 (5), 481–491 (in Chinese with
794 English abstract).
795 Cai, H.A., Xu, D.B., Li, B.F., Shao, L.Y., 2010. A study on Early Cretaceous volcanic effusion
796 periods and isotope chronology in western Liaoning. Coal Geol. Explor. 22 (12), 1–6 (in
797 Chinese with English abstract).
798 Chefetz, B., Deshmukh, A.P., Hatcher, P.G., Guthrie, E.A., 2000. Pyrene sorption by natural
799 organic matter. Environ. Sci. Technol. 34(14), 2925–2930.
800 https://doi.org/10.1021/es9912877.
801 Chen, F., Meng, X.Y., Ren, S.Q., Wu, C.L., 1988. The Early Cretaceous flora of Fuxin Basin
802 and Tiefa Basin, Liaoning Province. Geological Publishing House, Beijing, pp. 1–180. (in
803 Chinese).
804 Chen, F., Yang, G.X., Zhou, H.Q., 1981. Early Cretaceous flora in Fuxin Basin, Liaoning
805 Province. J. Earth Sci. (Chinese Ed.) 6(2), 39–55. (in Chinese with English abstract).
806 Coccioni, R., Sabatino, N., Frontalini, F., Gardin, S., Sideri, M., Sprovieri, M., 2014. The
807 neglected history of Oceanic Anoxic Event 1b: insights and new data from the Poggio le
808 Guaine section (Umbria-Marche Basin). Stratigraphy 11(3–4), 245–282.

809 Coiro, M., Doyle, J.A., Hilton, J., 2019. How deep is the conflict between molecular and fossil
810 evidence on the age of angiosperms? New Phytol. 223, 83–89.
811 https://doi.org/10.1111/nph.15708.
812 Couper, R.A., 1958. British Mesozoic microspores and pollen grains. Palaeontographica
813 Abteilung B 103, 75–179.
814 Deng, S.H., Chen, F., 2001. The Early Cretaceous Filicopsida from Northeast China.
815 Geological Publishing House, Beijing, pp. 1–249 (in Chinese).
816 Deng, S.H., Lu, Y.Z., Fan, R., Li, X., Fang, L.H., Liu, L., 2012. Cretaceous floras and
817 biostratigraphy of China. J. Stratigr. 36(2), 241–265.
818 Denis, E.H. Toney, J.L., Tarozo, R., Scott Anderson, R., Roach, L.D. Huang, Y.S., 2012.
819 Polycyclic aromatic hydrocarbons (PAHs) in lake sediments record historic fire events:
820 Validation using HPLC-fluorescence detection. Org. Geochem. 45, 7–17.
821 https://doi.org/10.1016/j.orggeochem.2012.01.005.
822 Diessel, C.F.K., 2010. The stratigraphic distribution of inertinite. Int. J. Coal Geol. 81, 251–
823 268. https://doi.org/10.1016/j.coal.2009.04.004.
824 Erbacher, J., Huber, B.T., Norris, R.D., Markey, M., 2001. Increased thermohaline stratification
825 as a possible cause for an ocean anoxic event in the Cretaceous period. Nature 409, 325–
826 327. https://doi.org/10.1038/35053041.
827 Fedo, C.M., Nesbitt, H.W., Young, G.M., 1995. Unravelling the effects of potassium
828 metasomatism in sedimentary rocks and paleosols, with implications for paleoweathering
829 conditions and provenance. Geology 23(10), 921–924.
830 Feild, T.S., Brodribb, T.J., Iglesias, A., Chatelet, D.S., Baresch, A., Jr., G.R.U., Gomez, B.,
831 Mohr, B.A.R., Coiffard, C., Kvacek, J., Jaramillo, C., 2011. Fossil evidence for
832 Cretaceous escalation in angiosperm leaf vein evolution. PNAS 108(20), 8363–8366.
833 https://doi.org/10.1073/pnas.1014456108.
834 Finkelstein, D.B., Pratt, L.M., Curtin, T.M., Brassell, S.C., 2005. Wildfires and seasonal aridity
835 recorded in Late Cretaceous strata from south-eastern Arizona, USA. Sedimentology 52,
836 587–599. https://doi.org/10.1111/j.1365-3091.2005.00712.x.
837 Friis, E.M., Pedersen, K.R., Crane, P.R., 2010. Cretaceous diversification of angiosperms in the
838 western part of the Iberian Peninsula. Rev. Palaeobot. Palyno. 162, 341–361.

https://doi.org/10.1016/j.revpalbo.2009.11.009.

Friedrich, O., Nishi, H., Pross, J., Schmiedl, G., Hemleben, C., 2005. Millenial- to Centennial-Scale Interruptions of the Oceanic Anoxic Event 1b (Early Albian, mid-Cretaceous) Inferred from Benthic Repopulation Events. Palaios 20, 64–77. https://doi.org/10.2110/palo.2003.p03-75.

Gao, Y., Ibarra, D.E., Caves Rugenstein, J.K., Chen, J.Q., Kukla, T., Methner, K., Gao, Y.F., Huang, H., Lin, Z.P., Zhang, L.M., Xi, D.P., Wu, H.C., Carroll, A.R., Graham, S.A., Chamberlain, C.P., Wang, C.S., 2021. Terrestrial climate in mid-latitude East Asia from the latest Cretaceous to the earliest Paleogene: A multiproxy record from the Songliao Basin in northeastern China. Earth-Science Reviews 216, 103572. https://doi.org/10.1016/j.earscirev.2021.103572.

Galloway, J.M., Sweet, A.R., Pugh, A., Schröder-Adams, C.J., Swindles, G.T., Haggart, J.W., Embry, A.F., 2012. Correlating middle Cretaceous palynological records from the Canadian High Arctic based on a section from the Sverdrup Basin and samples from the Eclipse Trough. Palynology 36, 277–302. https://doi.org/10.1080/01916122.2012.670411.

Glasspool, I.J., Edwards, D., Axe, L., 2004. Charcoal in the Silurian as evidence for the earliest wildfire. Geology 32(5), 381–383. https://doi.org/10.1130/G20363.1.

Glasspool, I.J., Scott, A.C., 2010. Phanerozoic concentrations of atmospheric oxygen reconstructed from sedimentary charcoal. Nat. Geosci. 3, 627–630. https://doi.org/10.1038/NGEO923.

Glasspool, I.J., Scott, A.C., Waltham, D., Pronina, N., Shao, L.Y., 2015. The impact of fire on the Late Paleozoic Earth system. Front. Plant Sci. 6, 756. https://doi.org/10.3389/fpls.2015.00756.

Grice, K., Nabbefeld, B., Maslen, E., 2007. Source and significance of selected polycyclic aromatic hydrocarbons in sediments (Hovea-3 well, Perth Basin, Western Australia) spanning the Permian–Triassic boundary. Org. Geochem. 38, 1795–1803. https://doi.org/10.1016/j.orggeochem.2007.07.001.

Guo, Z.Y., 1988. Relationship between alluvial fan-delta depositional system and coal accumulation of Shahai Formation in Fuxin Basin. Coal Geol. Explor. 16(4), 2–7. (in Chinese).

869 Handoh, I.C., Lenton, T.M., 2003. Periodic mid-Cretaceous oceanic anoxic events linked by
870 oscillations of the phosphorus and oxygen biogeochemical cycles. Global Biogeochem.
871 Cy. 17(4), 1092. https://doi.org/10.1029/2003GB002039.
872 Harland, M., Francis, J.E., Brentnall, S.J., Beerling, D.J., 2007. Cretaceous (Albian–Aptian)
873 conifer wood from Northern Hemisphere high latitudes: Forest composition and
874 palaeoclimate. Rev. Palaeobot. Palyno. 143, 167–196.
875 https://doi.org/10.1016/j.revpalbo.2006.07.005.
876 Haworth, M., Hesselbo, S.P., McElwain, J.C., Robinson, S.A., Brunt, J.W., 2005. Mid-
877 Cretaceous pCO_2 based on stomata of the extinct conifer *Pseudofrenelopsis*
878 (Cheirolepidiaceae). Geology 33(9), 749–752. https://doi.org/10.1130/G21736.1.
879 He, H.Y., Wang, X.L., Zhou, Z.H., Wang, F., Boven, A., Shi, G.H., Zhu, R.X., 2004. Timing
880 of the Jiufotang Formation (Jehol Group) in Liaoning, northeastern China, and its
881 implications. Geophys. Res. Lett. 31, 261–268. https://doi.org/10.1029/2004GL019790.
882 He, T., Lamont, B.B., 2018. Baptism by fire: the pivotal role of ancient conflagrations in
883 evolution of the Earth's flora. Natl. Sci. Rev. 5, 237–254.
884 https://doi.org/10.1093/nsr/nwx041.
885 Heimhofer, U., Hochuli, P.A., Herrle, J.O., Weissert, H., 2006. Contrasting origins of Early
886 Cretaceous black shales in the Vocontian basin: Evidence from palynological and
887 calcareous nannofossil records. Palaeogeogr. Palaeoclimatol. Palaeoecol. 235, 93–109.
888 https://doi.org/10.1016/j.palaeo.2005.09.025.
889 Herrle, J.O., 2002. Mid-Cretaceous paleoceanographic and paleoclimatologic implications on
890 black shale formation of the Vocontian Basin and Atlantic: evidence from calcareous
891 nannofossils and stable isotopes. Tübinger Mikropaläontologische Mitteilungen 27, 1–
892 114.
893 Herrle, J.O., Kößler, P., Friedrich, O., Erlenkeuser, H., Hemleben, C., 2004. High-resolution
894 carbon isotope records of the Aptian to Lower Albian from SE France and the Mazagan
895 Plateau (DSDP Site 545): a stratigraphic tool for paleoceanographic and paleobiologic
896 reconstruction. Earth Planet Sci. Lett. 218(1), 149–161. https://doi.org/10.1016/S0012-
897 821X(03)00646-0.
898 Herrle, J.O., Schroder-Adams, C.J., Davis, W., Pugh, A.T., Galloway, J.M., Fath, J., 2015. Mid-

899 Cretaceous High Arctic stratigraphy, climate, and Oceanic Anoxic Events. Geology 43(5),
900 403–406. https://doi.org/10.1130/G36439.1.
901 Hilton, J., Bateman, R.M., 2006. Pteridosperms are the backbone of seed–plant phylogeny.
902 Journal of the Torrey Botanical Society 133, 119–168. https://doi.org/10.3159/1095-
903 5674(2006)133[119:PATBOS]2.0.CO;2.
904 Hou, H.H., Shao, L.Y., Tang, Y., Li, Y.N., Liang, G.D., Xin, Y.L., Zhang, J.Q., 2020. Coal seam
905 correlation in terrestrial basins by sequence stratigraphy and its implications for
906 palaeoclimate and palaeoenvironment. J. Earth Sci. https://doi.org/10.1007/s12583-020-
907 1069-4.
908 Hower, J.C., O'Keefe, J.M.K., Wagner, N.J., Dai, S.F., Wang, X.B., Xue, W.F., 2013. An
909 investigation of Wulantuga coal (Cretaceous, Inner Mongolia) macerals: Paleopathology
910 of faunal and fungal invasions into wood and the recognizable clues for their activity. Int.
911 J. Coal Geol. 114(30), 44–53. https://doi.org/10.1016/j.coal.2013.04.005.
912 Hong, S.K., Lee, Y.I., 2012. Evaluation of atmospheric carbon dioxide concentrations during
913 the Cretaceous. Earth Planet. Sci. Lett. 327-328, 23–28.
914 https://doi.org/10.1016/j.epsl.2012.01.014.
915 Hu, G., Hu, W., Cao, J., Yao, S., Liu, W., Zhou, Z., 2014. Fluctuation of organic carbon
916 isotopes of the Lower Cretaceous in coastal southeastern China: Terrestrial response to the
917 Oceanic Anoxic Events (OAE 1b). Palaeogeogr. Palaeoclimatol. Palaeoecol. 399, 352–
918 362. http://dx.doi.org/10.1016/j.palaeo.2014.01.027.
919 Huang, J.G., Bergeron, Y., Denneler, B., Berninger, F., Tardif, J., 2007. Response of forest trees
920 to increased atmospheric CO_2. Crit. Rev. Plant Sci. 26, 265–283.
921 https://doi.org/10.1080/07352680701626978.
922 Huber, B.T., Macleod, K.G., Gröcke, D.R., Kucera, M., 2011. Paleotemperature and
923 paleosalinity inferences and chemostratigraphy across the Aptian/Albian boundary in the
924 subtropical North Atlantic. Paleoceanography 26, PA4221.
925 http://dx.doi.org/10.1029/2011PA002178.
926 Jasper, A., Agnihotri, D., Tewari, R., Spiekermann, R., Pires, E.F., Rosa, Á.A.S.D., Uhl, D.,
927 2016. Fires in the mire: repeated fire events in Early Permian ‘peat forming’ vegetation of
928 India. Geol. J. 52(6), 955-969. http://dx.doi.org/10.1002/gj.2860.

Jenkyns, H.C., 2010. Geochemistry of oceanic anoxic events. Geochem. Geophy. Geosy. 11(3), 1–30. http://dx.doi.org/10.1029/2009GC002788.

Jiang, C., Alexander, R., Kagi, R.I., Murray, A.P., 1998. Polycyclic aromatic hydrocarbons in ancient sediments and their relationships to palaeoclimate. Org. Geochem. 29(5-7), 1721–1735. http://dx.doi.org/10.1016/S0146-6380(98)00083-7.

Jones, T.P., Chaloner, W.G., 1991. Fossil charcoal, its recognition and palaeoatmospheric significance. Palaeogeogr. Palaeoclimatol. Palaeoecol. 97(1–2), 39–50. https://doi.org/10.1016/0031-0182(91)90180-Y.

Jones, T.P., Scott, A.C., Cope, M., 1991. Reflectance measurements and the temperature of formation of modern charcoals and implications for studies of fusain. Bulletin de la Société Géologique de France 162(2), 193–200.

Jones, T.P., 1994. New morphological and chemical evidence supporting a wildfire origin for fusain from comparisons with modern charcoal. In: Collinson, M. and Scott, A.C. (Eds.), Studies in Palaeobotany and Palynology in Honour of Professor W. G. Chaloner, F.R.S., Special Papers in Palaeontology, vol. 49. Palaeontological Association, London, pp. 113–123.

Jones, T.P., 1996. A fire-related origin for fusain: comparisons with the physicochemical characteristics of laboratory produced charcoal. Neues Jahrbuch für Geologie und Paläontologie - Abhandlungen 202(2), 159–168. https://doi.org/10.1127/njgpa/202/1996/159.

Jones, T.P., 1997. Fusain in Late Jurassic sediments from Witch Ground Graben, North Sea, U.K. Mededelingen Nederlands Instituut voor Toegepaste Geowetenschappen TNO 58, 93–103.

Kang, S.L., Shao, L.Y., Qin, L.Z., Li, S.X., Liu, J.S., Shen, W.C., Chen, X.D., Eriksson, K.A., Zhou, Q.Y., 2020. Hydrocarbon generation potential and depositional setting of Eocene oil-prone coaly source rocks in the Xihu Sag, East China Sea Shelf Basin. ACS Omega 5(50), 32267–32285. https://dx.doi.org/10.1021/acsomega.0c04109.

Korasidis, V.A., Wagstaff, B.E., Gallagher, S.J., Duddy, I.R., Tosolini, AMP., Cantrill, D.J., Norvick, M.S., 2016. Early angiosperm diversification in the Albian of southeast Australia: implications for flowering plant radiation across eastern Gondwana. Rev.

959 Palaeobot. Palyno. 232: 61–80. https://doi.org/10.1016/j.revpalbo.2016.04.005.
960 Leng, Q., Friis, E.M., 2003. *Sinocarpus decussates* gen. et sp. nov., a new angiosperm with
961 basally syncarpous fruits from the Yixian Formation of Northeast China. Plant Syst. Evol.
962 241, 77–88.
963 Li, J.H., Jiang, H.F., 2013. Global palaeoplate reconstruction, lithofacies palaeogeography and
964 paleoenvironmental atlas. Geological Publishing House, Beijing, pp. 1–127 (in Chinese).
965 Li, S.T., 1988. Fault basin analysis and coal accumulation. Geological Publishing House,
966 Beijing, pp. 1–367. (in Chinese).
967 Li, X.H., Wei, Y.S., Li, Y.X., Zhang, C.K., 2016. Carbon isotope records of the early Albian
968 oceanic anoxic event (OAE) 1b from eastern Tethys (southern Tibet, China). Cretaceous
969 Res. 62, 109–121. https://doi.org/10.1016/j.cretres.2015.08.015.
970 Liu, J.Y., Wang, S.Y., Yin, J.H., 1992, Petroleum geological character of Fuxin Basin. Oil Gas
971 Geol. 13(4), 450–457 (in Chinese with English abstract).
972 Liu, G.Q., Zhang, G., Li, X.D., Li, J., Peng, X.Z., Qi, S.H., 2005. Sedimentary record of
973 polycyclic aromatic hydrocarbons in a sediment core from the Pearl River Estuary, South
974 China. Mar. Pollut. Bull. 51, 912–921.
975 https://dx.doi.org/10.1016/j.marpolbul.2005.02.038.
976 Liu, Z.Y., Selby, D., Hackley, P.C., Jeffrey Over, D., 2020. Evidence of wildfires and elevated
977 atmospheric oxygen at the Frasnian–Famennian boundary in New York (USA):
978 Implications for the Late Devonian mass extinction. Geol. Soc. Am. Bull. 132 (9-10),
979 2043–2054. https://doi.org/10.1130/B35457.1.
980 Lu, J., Zhou, K., Yang, M.F., Eley, Y., Shao, L.Y., Hilton, J., 2020. Terrestrial organic carbon
981 isotopic composition ($\delta^{13}C_{org}$) and environmental perturbations linked to Early Jurassic
982 volcanism: evidence from the Qinghai-Tibet Plateau of China. Glob. Planet. Chang. 195,
983 103331. https://doi.org/10.1016/j.gloplacha.2020.103331.
984 Lu, M., Ikejiri, T., Lu, Y.H., 2021. A synthesis of the Devonian wildfire record: Implications
985 for paleogeography, fossil flora, and paleoclimate. Palaeogeogr. Palaeoclimatol.
986 Palaeoecol. 571, 110321. https://doi.org/10.1016/j.palaeo.2021.110321.
987 Ludvigson, G.A., Joeckel, R.M., Gonzalez, L.A., Gulbranson, E.L., Rasbury, E.T., Hunt, G.J.,
988 Kirkland, J.I., Madsen, S., 2010. Correlation of AptianeAlbian carbon isotope excursions in

continental strata of the Cretaceous foreland basin, eastern Utah, U.S.A. J. Sed. Res. 80, 955–974. http://dx.doi.org/10.2110/jsr.2010.086.

Marynowski, L., Kurkiewicz, S., Rakocinski, M., Simoneit, B.R.T., 2011. Effects of weathering on organic matter: I. Changes in molecular composition of extractable organic compounds caused by paleoweathering of a Lower Carboniferous (Tournaisian) marine black shale. Chem. Geol. 285, 144–156. https://dx.doi.org/10.1016/j.chemgeo.2011.04.001.

Marynowski, L., Simoneit, B.R.T., 2009. Widespread upper Triassic to Lower Jurassic wildfire records from Poland: Evidence from charcoal and pyrolytic polycyclic aromatic hydrocarbons. Palaios 24, 785–798. https://dx.doi.org/10.2110/palo.2009.p09-044r.

Matsumoto, H., Kuroda, J., Coccioni, R., Frontalini, F., Sakai, S., Ogawa, N.O., Ohkouchi, N., 2020. Marine Os isotopic evidence for multiple volcanic episodes during Cretaceous Oceanic Anoxic Event 1b. Sci. Rep. 10, 12601. https://doi.org/10.1038/s41598-020-69505-x.

Meng, Y., Liu, X.H., Lu, S.Y., Zhang, T.T., Jin, B.C., Wang, Q., Tang, Z.R., Liu, Y., Guo, X.H., Zhou, J.L., Xi, B.D., 2019. A review on occurrence and risk of polycyclic aromatic hydrocarbons (PAHs) in lakes of China. Sci. Total Environ. 651, 2497–2506. https://doi.org/10.1016/j.scitotenv.2018.10.162.

Mills, B.J.W., Belcher, C.M., Lenton, T.M., Newton, R.J., 2016. A modeling case for high atmospheric oxygen concentrations during the Mesozoic and Cenozoic. Geology, 44(12), 1023–1026. https://doi.org/10.1130/G38231.1.

Moore, T.A., Moroeng, O.M., Shen, J., Esterle, J.S., Pausch, R.C., 2021. Using carbon isotopes and organic composition to decipher climate and tectonics in the Early Cretaceous: An example from the Hailar Basin, Inner Mongolia, China. Cretaceous Res. 118, 104674. https://doi.org/10.1016/j.cretres.2020.104674.

Murchison, D.G., Raymond, A.C., 1989. Igneous activity and organic maturation in the Midland Valley of Scotland. Int. J. Coal Geol. 14, 47–82. https://doi.org/10.1016/0166-5162(89)90078-5.

Navarro-Ramirez, J.P., Bodin, S., Heimhofer, U., Immenhauser, A., 2015. Record of Albian to early Cenomanian environmental perturbation in the eastern sub-equatorial Pacific. Palaeogeogr. Palaeoclimatol. Palaeoecol. 423, 122–137.

http://dx.doi.org/10.1016/j.palaeo.2015.01.025.
Nesbitt, H.W., Young, G.M., 1982. Early Proterozoic climates and plate motions inferred from major element chemistry of lutites. Nature 299, 715–717. https://doi.org/10.1038/299715a0.
Oakley, O., Falcon-Lang, H.J., 2009. Morphometric analysis of Cretaceous (Cenomanian) angiosperm woods from the Czech Republic. Rev. Palaeobot. Palyno. 153, 375–385. https://doi.org/10.1016/j.revpalbo.2008.10.006.
Page, D.S., Boehm, P.D., Douglas, G.S., Bence, A.E., Burns, W.A., Mankiewicz, P.J.,1999. Pyrogenic polycyclic aromatic hydrocarbons in sediments record past human activity: A case study in Prince William Sound, Alaska. Mar. Pollut. Bull. 38(4), 247–260. https://doi.org/10.1016/S0025-326X(98)00142-8.
Parker, A. 1970. An index of weathering for silicate rocks. Geol. Mag. 107(6), 501–504. https://doi.org/10.1017/S0016756800058581.
Petersen, H.I., Lindstrom, S., 2012. Synchronous wildfire activity rise and mire deforestation at the Triassic–Jurassic boundary. PLOS ONE 7(10), e47236. https://doi.org/10.1371/journal.pone.0047236.
Royer, D.L., Miller, I.M., Peppe, D.J., Hickey, L.J., 2010. Leaf economic traits from fossils support a weedy habit for early angiosperms. Am. J. Bot. 97(3), 438–445. https://doi.org/10.3732/ajb.0900290.
Sabatino, N., Coccioni, R., Manta, D.S., Baudin, F., Vallefuoco, M., Traina, A., Sprovieri, M., 2015. High-resolution chemostratigraphy of the late Aptian-early Albian oceanic anoxic event (OAE 1b) from the Poggio le Guaine section (Umbria–Marche Basin, central Italy). Palaeogeogr. Palaeoclimatol. Palaeoecol. 426, 319–333. https://doi.org/10.1016/j.palaeo.2015.03.009.
Scott, A.C., 2002. Coal petrology and the origin of coal macerals: a way ahead? Int. J. Coal Geol. 50, 119–134.
Scott, A.C., 2010. Charcoal recognition, taphonomy and uses in palaeoenvironmental analysis. Palaeogeogr. Palaeoclimatol. Palaeoecol. 291, 11–39. https://doi.org/10.1016/j.palaeo.2009.12.012.
Scott, A.C., Glasspool, I.J., 2006. The diversification of Paleozoic fire systems and fluctuations

in atmospheric oxygen concentration. PNAS 103(29), 10861–10865. https://doi.org/10.1073/pnas.0604090103.

Scott, A.C., Glasspool, I.J., 2007. Observations and experiments on the origin and formation of inertinite group macerals. Int. J. Coal Geol. 70, 53–66. https://doi.org/10.1016/j.coal.2006.02.009.

Scott, A.C., Jones, T.P., 1994. The nature and influence of fire in Carboniferous ecosystems. Palaeogeogr. Palaeoclimatol. Palaeoecol. 106, 91–112. https://doi.org/10.1016/0031-0182(94)90005-1.

Sender, L.M., Villanueva-Amadoz, U., Pons, D., Diez, J.B., Ferrer, J., 2014. Singular taphonomic record of a wildfire event from middle Albian deposits of Escucha Formation in northeastern of Spain. Hist. Biol. 27(3–4), 442–452. https://doi.org/10.1080/08912963.2014.895827.

Shao, L.Y., Wang, H., Yu, X.H., Lu, J., Zhang, M.Q., 2012. Paleo-fires and atmospheric oxygen levels in the latest Permian: vidence from maceral compositions of coals in Eastern Yunnan, Southern China. Acta Geol. Sinica 86(4), 949–962.

Song, Z.H., 1986. Review on the study of early Cretaceous angiosperm pollen in China. Acta Micropalaeontologica Sinica 3(4), 373–380 (in Chinese with English abstract).

Su, N., Zhu, G., Wu, X. D., Yin, H., Lu, Y.C., Zhang, S., 2021. Back-arc tectonic tempos: Records from Jurassic–Cretaceous basins in the eastern North China Craton. Gondwana Res. 90, 241–257. https://doi.org/10.1016/j.gr.2020.12.002.

Sullivan, R.F., Boduszynski, M.M., Fetzer, J.C., 1989. Molecular transformations in hydrotreating and hydrocracking. Energ. Fuel. 3, 603–612. https://doi.org/10.1021/ef00017a013.

Sun, G., Zheng, S.L., Sun, X.K., He, C.Q., Pu, T.Y., Shang, Y.K., Zhang, C.B., Yu, Z.Y., Zhao, Y.H., 1992. Recent advance in the research of the strata near the Jurassic-Cretaceous boundary in eastern Heilongjiang. J. Stratigr. 16(1), 49–54 (in Chinese with English abstract).

Sun, G., Dilcher, D.L., Zheng, S.L., Zhou, Z.K., 1998. In search of the first flower: a Jurassic angiosperm, *Archaefructus*, from Northeast China. Science 282, 1692–1695.

Sun, G., Ji, Q., Dilcher, D.L., Zheng, S.L., Nixon, K., Wang, X.F., 2002. Archaefructaceae, a

new basal angiosperm family. Science 296, 899–904. https://doi.org/10.1126/science.1069439.

Sun, W. L. (2006). China coalbed methane basins atlas. Geological Publishing House, Beijing, pp. 1–233. (in Chinese).

Sun, Y.W., Li, X., G.W., Liu, H., Zhang, Y.L., 2016. Aptian and Albian atmospheric CO_2 changes during oceanic anoxic events Evidence from fossil *Ginkgo* cuticles in Jilin Province, Northeast China. Cretaceous Res. 62, 130–141. https://doi.org/10.1016/j.cretres.2015.12.007.

Tao, M.H., Cui, Z.Q., Chen, G.Q., 2013. Mesozoic sporo-pollen assemblages and climate fluctuations in northeastern China. Acta Micropalaeontologica Sinica 30(3), 275–287 (in Chinese with English abstract).

Thompson, K.L., Picard, C.R., Chan, H.M., 2017. Polycyclic aromatic hydrocarbons (PAHs) in traditionally harvested bivalves in northern British Columbia, Canada. Mar. Pollut. Bull. 121, 390–399. https://doi.org/10.1016/j.marpolbul.2017.06.018.

Trabucho Alexandre, J., van Gilst, R.I., Rodríguez-López, J.P., De Boer, P.L., 2011. The sedimentary expression of oceanic anoxic event 1b in the North Atlantic. Sedimentology 58, 1217–1246. https://doi.org/10.1111/j.1365-3091.2010.01202.x.

Tsikos, H., Karakitsios, V., van Breugel, Y., Walsworth-Bell, B., Bombardiere, L., Petrizzo, M.R., Damst, J.S.S., Schouten, S., Erba, E., Silva, I.P., Farrimond, P., Tyson, R.V., Jenkyns, H.C., 2004. Organic-carbon deposition in the Cretaceous of the Ionian Basin, NW Greece: the Paquier Event (OAE 1b) revisited. Geol. Mag. 141(4), 401–416. http://dx.doi.org/10.1017/S0016756804009409.

Wan, X.Q., Li, G., Huang, Q.H., Xi, D.P., Chen, P.J., 2013. Division and correlation of terrestrial Cretaceous stages in China. J. Stratigr. 37(4), 457–471 (in Chinese with English abstract).

Wang, W.F., Lu, S.K., Guo, Y.X., Sun, Y.P., 1998. Tectonic geometry and type of traps in Fuxin Basin. J. Univ. Petrol. China 22(3), 29–33 (in Chinese with English abstract).

Wang, D.D., Yin, L.S., Shao, L.Y., Lv, D.W., Liu, H.Y., Wang, S., Dong, G.Q., 2021a. Characteristics and evolution of inertinite abundance and atmospheric pO_2 during China's coal-forming periods. J. Palaeogeogr. 10, 13. https://doi.org/10.1186/s42501-021-00090-

4.

Wang, D.D., Mao, Q., Dong, G.Q., Yang, S.P., Lv, D.W., Yin, L.S., 2019a. The Primary investigation of the genetic mechanism of inertinite in the Middle Jurassic inertinite-rich coal seams of the southern Ordos Basin. J. Geol. Res. 1(3), 1–15.

Wang, S., Shao, L.Y., Yan, Z.M., Shi, M.J., Zhang, Y.H., 2019b. Characteristics of Early Cretaceous wildfires in peat-forming environment, NE China. J. Palaeogeogr. 103(7), 1653–1690. https://doi.org/10.1186/s42501-019-0035-5.

Wang, S., Shao, L.Y., Li, J.X., Li, J.A., Jones , T., Zhu, M.Y., Zhou, J.M., 2021b. Coal petrology of the Yimin Formation (Albian) in the Hailar Basin, NE China: Paleoenvironments and wildfires during peat formation. Cretaceous Res. 124, 104815. https://doi.org/10.1016/j.cretres.2021.104815.

Wildman, R.A, Hickey, L.J., Dickinson, M.B., Berner, R.A., Robinson, J.M., Dietrich, M., Essenhigh, R.H., Wildman, C.B., 2004. Burning of forest materials under late Paleozoic high atmospheric oxygen levels. Geology, 32(5), 457–460. https://doi.org/10.1130/G20255.1.

Wu, F.Y., Xu, Y.G., Zhu, R.X., Zhang, G.W., 2014. Thinning and destruction of the cratonic lithosphere: a global perspective. Sci. China Earth Sci. 57 (2), 2878–2890.

Xi, D.P., Wan, X.Q., Li, G.B., Li, G., 2019. Cretaceous integrative stratigraphy and timescale of China. Sci. China Earth Sci. 62(1), 256–286. https://doi.org/10.1007/s11430-017-9262-y.

Xu, D.B., Li, B.F., Chang, Z.L., Zhang, J.B., Cai, H.A., 2012. Study of U–Pb isotopic age and sequence of the Cretaceous volcanic rocks and coal-searching in Fuxian–Zhangwu–Heishan area, western Liaoning Province. Earth Sci. Front. 19 (6), 155–166 (in Chinese with English abstract).

Xu, X.T., Shao, L.Y., 2018. Limiting factors in utilization of chemical index of alteration of mudstones to quantify the degree of weathering in provenance. J. Palaeogeogr. 20(3), 515–522. (in Chinese with English abstract).

Xu, X.T., Shao, L.Y., Lan, B., Wang, S., Hilton, J., Qin, J., Hou, H., Zhao, J., 2020a. Continental chemical weathering during the Early Cretaceous Oceanic Anoxic Event (OAE 1b): a case study from the Fuxin fluvio-lacustrine basin, Liaoning Province, NE China. J.

Palaeogeogr. 9(2), 246–266. https://doi.org/10.1186/s42501-020-00056-y.

Xu, X.T., Shao, L.Y., Fu, Y.F., Wang, D.D., Cai, H.A., Qin, J.Y., Hou, H.H., Zhao. J., 2020b. Sequence palaeogeography, lacustrine basin evolution, and coal accumulation in the Lower Cretaceous Fuxin continental faulted basin, China. Geol. J. 55(2), 1195–1215. https://doi.org/10.1002/gj.3483.

Xu, X.T., Shao, L.Y., Eriksson, K.A., Pang, B., Wang, S., Yang, C.X., Hou, H.H., 2022. Terrestrial records of the early Albian Ocean Anoxic Event: Evidence from the Fuxin lacustrine basin, NE China. Geosci. Front. 13(1), 101275. https://doi.org/10.1016/j.gsf.2021.101275.

Xu, Y., Uhl, D., Zhang, N., Zhao, C., Qin, S., Liang, H., Sun, Y., 2020c. Evidence of widespread wildfires in coal seams from the Middle Jurassic of Northwest China and its impact on paleoclimate. Palaeogeogr. Palaeoclimatol. Palaeoecol. 559, 109819. https://doi.org/10.1016/j.palaeo.2020.109819.

Yan, Z.M., Shao, L.Y., Glasspool, I.J., Wang, J., Wang, X.T., Wang, H., 2019. Frequent and intense fires in the final coals of the Paleozoic indicate elevated atmospheric oxygen levels at the onset of the End-Permian Mass Extinction Event. Int. J. Coal Geol. 207, 75–83. https://doi.org/10.1016/j.coal.2019.03.016.

Yang, Y.K., 1996. Atlas for Coal Petrography of China. China University of Mining and Technology Press, Xuzhou, pp. 1–99. (in Chinese).

Zakir Hossain, H.M., Sampei, Y., Roser, B.P., 2013. Polycyclic aromatic hydrocarbons (PAHs) in late Eocene to early Pleistocene mudstones of the Sylhet succession, NE Bengal Basin, Bangladesh: Implications for source and paleoclimate conditions during Himalayan uplift. Org. Geochem. 56, 25–39. https://doi.org/10.1016/j.orggeochem.2012.12.001.

Zhang, J., 2003. Geothermal resources hosting condition analysis, Dongliang District, Fuxin Basin. Coal Geol. China 15(6), 37–39. (in Chinese with English abstract).

Zhang, Q., Zhang, M.S., Li, X.B., Wang, Y.N., Liu, X.S., Zhang, M.M., 2016. Stratigraphic sequences and zircon U–Pb dating of Yixian Formation in Caozhuang area of Xingcheng，western Liaoning. Global Geol. 35(1), 51–65. (in Chinese with English abstract).

Zhang, Z.H., Wang, C.S., Lv, D.W., Hayd, W.W., Wang, T.T., Cao, S., 2020. Precession-scale climate forcing of peatland wildfires during the early middle Jurassic greenhouse period.

Glob. Planet. Chang. 184, 103051. https://doi.org/10.1016/j.gloplacha.2019.103051.

Zhao, X.D., Zheng, D.R., Wang, H., Fang, Y.N., Xue, N.H., Zhang, H.C., 2022. Carbon cycle perturbation and mercury anomalies in terrestrial Oceanic Anoxic Event 1b from Jiuquan Basin, NW China. Geological Society, London, Special Publications 521.

Zhou, W.F., Algeo, T.J., Luo, G.M., Ruan, X.Y., Chen, Z.Q., Xie, S.C., 2021. Hydrocarbon compound evidence in marine successions of South China for frequent wildfires during the Permian-Triassic transition. Glob. Planet. Chang. 200, 103472. https://doi.org/10.1016/j.gloplacha.2021.103472.

Zhou, Z.H., Barrett, P.M., Hilton, J., 2003. An exceptionally preserved Lower Cretaceous ecosystem. Nature 421, 807–814. https://doi.org/10.1038/nature01420.

Zhu, R.X., Lo, C.H., Shi, R.P., Shi, G.G., Pan, Y.X., Sha, J., 2004. Palaeointensities determined from the middle Cretaceous basalt in Liaoning Province, northeastern China. Phys. Earth Planet. In. 142, 49–59. https://doi.org/10.1016/j.pepi.2003.12.013.

Zhu, R.X., Zhang, H.F., Zhu, G., Meng, Q.R., Fan, H.R., Yang, J.H., Wu, F.Y., Zhang, Z.Y., Zheng, T.Y., 2017. Craton destruction and related resources. Int. J. Earth Sci. 106, 2233–2257.

Zhu, Z.M., Yan, J.F., Shen, B., Zhou, J.Y., 2007. Co-existing formation of multi-energy resources in the Fuxin Basin analysis from tectonic-thermal events. Adv. Earth Sci. 22(5), 468–479. (in Chinese with English abstract).

Figures and table captions

Fig. 1. Location of the Fuxin Basin. a. Outline map of China showing position of Fuxin Basin. b. Enlargement of the top right part of Figure 1a showing position of the Fuxin basin and tectonic features (modified after Zhu et al., 2007). c. Global palaeogeographic map of the early Cretaceous showing approximate location of study area (modified from the ~110 Ma map of the webpage https://deeptimemaps.com/global-paleogeography-and-tectonics-in-deep-time). Abbreviations: AfP = African Plate; AnP = Antarctic Plate; Arp = Arabian Plate; AuP = Australian Plate; CAP = Central Asian Plate; EP = European Plate; IP = Indian Plate; NAP = North America Plate; NCP = North China Plate; SAmP = South American Plate; SAsP = Southeast Asian Plate; SCP = South China Plate; SP = Siberian Plate.

Fig. 2. Geology and stratigraphy of the Fuxin Basin. a. Geologic map of the Fuxin Basin (modified after Sun, 2006); cross-section A-A' is modified from the interpreted seismic profile (Zhu et al., 2007; Su et al., 2021). b. Stratigraphic succession for the western Liaoning region during the Aptian–Albian interval with flora assemblages (Deng et al., 2012) and isotopic ages. Age sources: ①from Zhang et al. 2016; ②from Xu et al. 2012; ③from Su et al. 2021; ④ from He et al. 2004; ⑤from Xu et al. 2021; ⑥from Zhu et al. 2004. I, II, III and IV represent the first, second, third and fourth members of the Shahai Formation, respectively. Abbreviations: Flora assem. = Flora assemblages.

Fig. 3. Stratigraphic distribution of kerogen macerals from mudstone samples in borehole DY-1 from the Lower Cretaceous Shahai and Fuxin formations in the Fuxin Basin. The interpretation of the sedimentary environments and zircon U-Pb age is from Xu et al. (2022). Abbreviations: J. F. = Jiufotang Formation; S. F. = Sunjiawan Formation; Sed. en. = Sedimentary environments.

Fig. 4. Photomicrographs showing microstructural characteristics of kerogen macerals from borehole DY-1 in the early Cretaceous Fuxin Basin. a and b, sapropelinite (transmitted light, 600m and 1095.5m). c and d, vitrinite (transmitted light, 714.5m). e and f, conifer pollen (transmitted light and fluorescence, respectively, 714.5m). g. fern spore (transmitted light, 714.5m). h. conifer pollen (transmitted light, 413m). i. conifer pollen (transmitted light, 714.5m). j. conifer pollen (transmitted light, 856m). k, l and m, inertinite (transmitted light, 413m, 1146m and 946.3m).

Fig. 5. Photographs of macroscopic charcoal and plant fossils from borehole DY-1 and outcrops in the early Cretaceous Fuxin Basin. a. Small charcoal fragments with black color in sandstone, 541m. b. Charcoalified wood fragments in mudstone, 625.8m. c. Small charcoals showing long strips in fine sandstone, 847.5m. d-f. Lacustrine mudstone with abundant charred plant fossil fragments, the depth is 862.2m, 919.8m and 920.5m respectively. g. Small charcoalified wood fragments in lacustrine mudstone, 1093.8m. h. Charred tree trunk fossil in lacustrine mudstone, 1135.9m. i. Charcoalified tree trunk fossil and angular wood fragments

Haizhou open-pit coal mine section; the hammer is 30 cm long. j. Abundant charcoal fragments in sandstones showing cubic blocks of charcoalified wood, Haizhou open-pit coal mine section; the hammer is 30 cm long. k. Grey mudstone with cycad fossil fragments, 540m. l. Grey siltstone with cycad fossil fragments, Haizhou open-pit coal mine section.

Fig. 6. Photomicrographs of inertinite contents in mudstone from borehole DY-1 in the early Cretaceous Fuxin Basin. a. Inertinite with compressed and broken cell walls, reflected light, 413m. b and c, inertinite, reflected light, 459m and 800m. d. Inertinite with regular and complete arrangement of cellular structure with relatively high reflectance, 1095.5m.

Fig. 7. Scanning electron micrographs of inertinite in mudstone from borehole DY-1; early Cretaceous Fuxin Basin. a. Detail of tracheids with uniseriate, contiguous, circular pits in walls, 458.6m. b. Longitudinal section of tracheids showing homogenized cell walls, 625.8m. c. Transverse section of vessels with high density, 847.5m. d. Longitudinal section of tracheids with tracheids broken by compaction, 868.9m. e. Cross-section with homogenized cell walls, 919.8m. f. Cross-section showing relatively well-preserved tracheids with cellular structure, 1093.8m.

Fig. 8. Total ion current traces of aromatic hydrocarbon fractions for the ten mudstone samples in borehole DY-1 from the early Cretaceous Fuxin Basin. Structures for selected PAHs show the total ion current chromatograms of samples DY-1-5, DY-1-8 and DY-1-16. IS-internal standard; VI-Phenanthrene; VII-Anthracene; VIII-Retene; IX-Fluoranthene; X-Benzo[a]fluorine; XI-Benzo[b]fluorine; XII-Pyrene; XIII-Benz(a)anthracene; XIV- Chrysene; XV-Benzofluoranthenes; XVI-Benzo(e)pyrene; XVII-Benzo(a)pyrene; XVIII-Perylene.

Fig. 9. Carbon isotopic correlation of the OAE1b event between marine and terrestrial successions. Carbon isotopic data collected from the borehole DY-1 in the Fuxin Basin, NE China. Data collated for the Fuxin terrestrial basin from Xu et al. (2022), the Chong'an terrestrial section in SE China from Hu et al. (2014), the Hanxiagou terrestrial section in NW China from Zhao et al. (2022), the marine Vocontian Basin (SE France) from Herrle et al.

(2004), the marine Poggio le Guaine Section from Matsumoto et al. (2020), the marine Andean Basin, northern Peru from Navarro-Ramirez et al. (2015) and ODP site 1049 off northern Florida on the Blake Nose escarpment from Huber et al. (2011).

Fig. 10. Correlation of kerogen macerals, wildfire types, organic carbon isotopes ($\delta^{13}C_{org}$) and total organic carbon (TOC) across the early Albian OAE 1b. Depth locations are shown in Fig. 4. The zircon U-Pb age, organic carbon isotopes ($\delta^{13}C_{org}$) and total organic carbon (TOC) is from Xu et al. (2022). Abbreviations: J. F. = Jiufotang Formation; S. F. = Sunjiawan Formation.

Fig. 11. Predictions of pO_2 in Unit C during the early Albian in the Fuxin Basin based on the model proposed by Glasspool et al. (2015). S-shaped curves are assumed to ensure a smooth transition from 0% inertinite at low oxygen levels to 100% inertinite at high oxygen levels. However, the curve above 35% pO_2 is relatively unimportant as plant biomass can still burn so readily as to be incompatible with sustained plant growth (Jones and Chaloner, 1991). The two blue curves represent the error interval. Red curve represents the best estimate for pO_2 level. Abbreviations: Min. = minimum; Max. = maximum; Aver. = average.

Fig. 12. Schematic model illustrating possible relationship between wildfire activity and anoxia in the Fuxin lacustrine basin during the early Albian OAE 1b. Wildfires and associated post-fire erosion intensified the transport rate of nutrients and organic matter from continents into lakes under conditions of intensified continental chemical weathering, thereby contributing to eutrophication and anoxia in lacustrine and contemporaneous oceanic systems.

Table 1 Kerogen macerals and inertinite reflectance values of mudstone samples from the Lower Cretaceous Shahai and Fuxin formations in the Fuxin Basin.

Table 2 Concentration of the PAHs of ten mudstones from the early Cretaceous Fuxin Basin.

Fig. 1

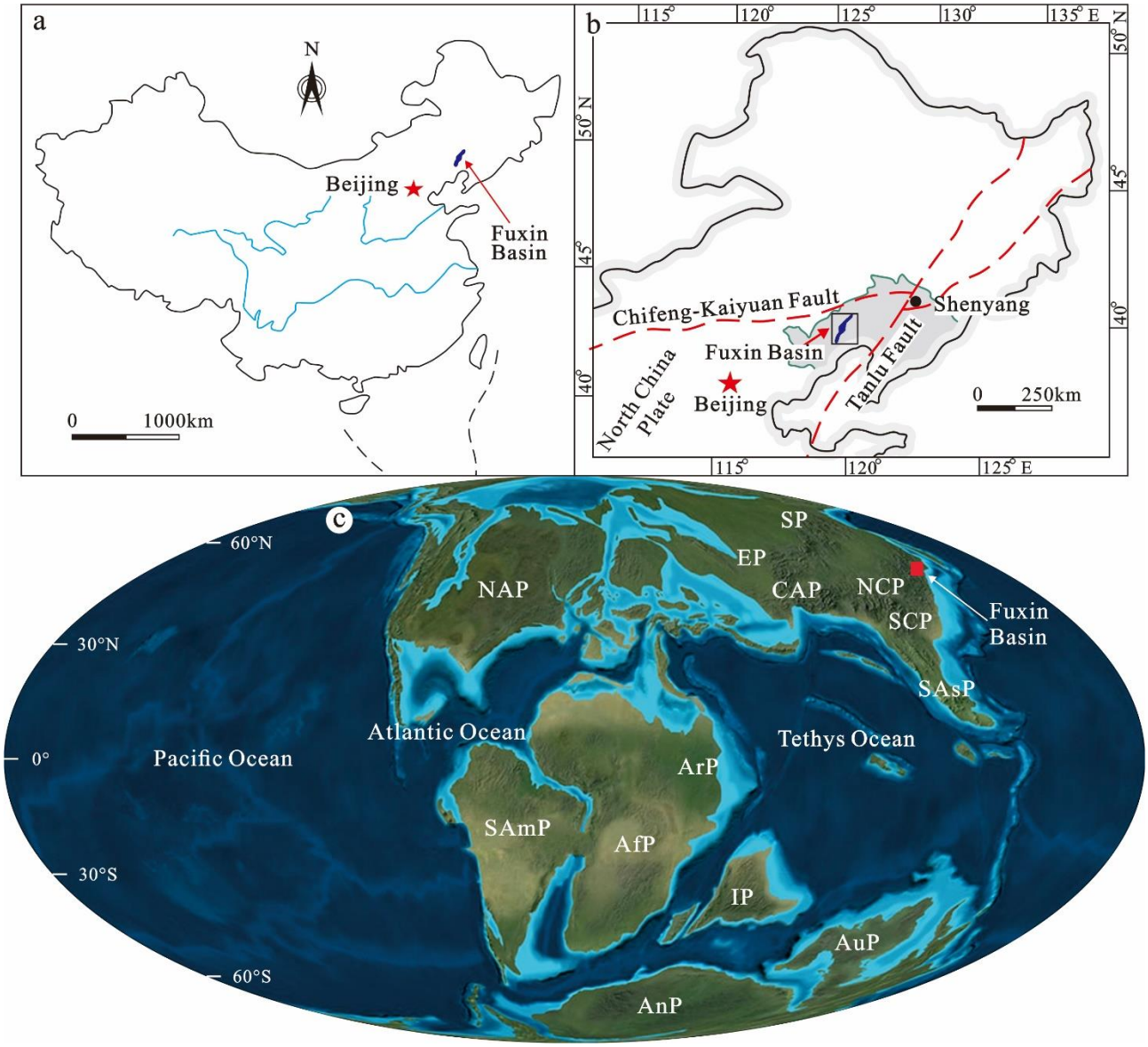
a
N
Beijing
Fuxin Basin
0 1000km
b
115° 120° 125° 130° 135° E
50° N
45°
40°
Chifeng-Kaiyuan Fault
Shenyang
Fuxin Basin
Tanlu Fault
North China Plate
Beijing
0 250km
c
60°N
30°N
0°
30°S
60°S
SP
EP
NAP
CAP
NCP
SCP
Fuxin Basin
SAsP
Atlantic Ocean
Tethys Ocean
Pacific Ocean
ArP
SAmP
AfP
IP
AuP
AnP

Fig. 2

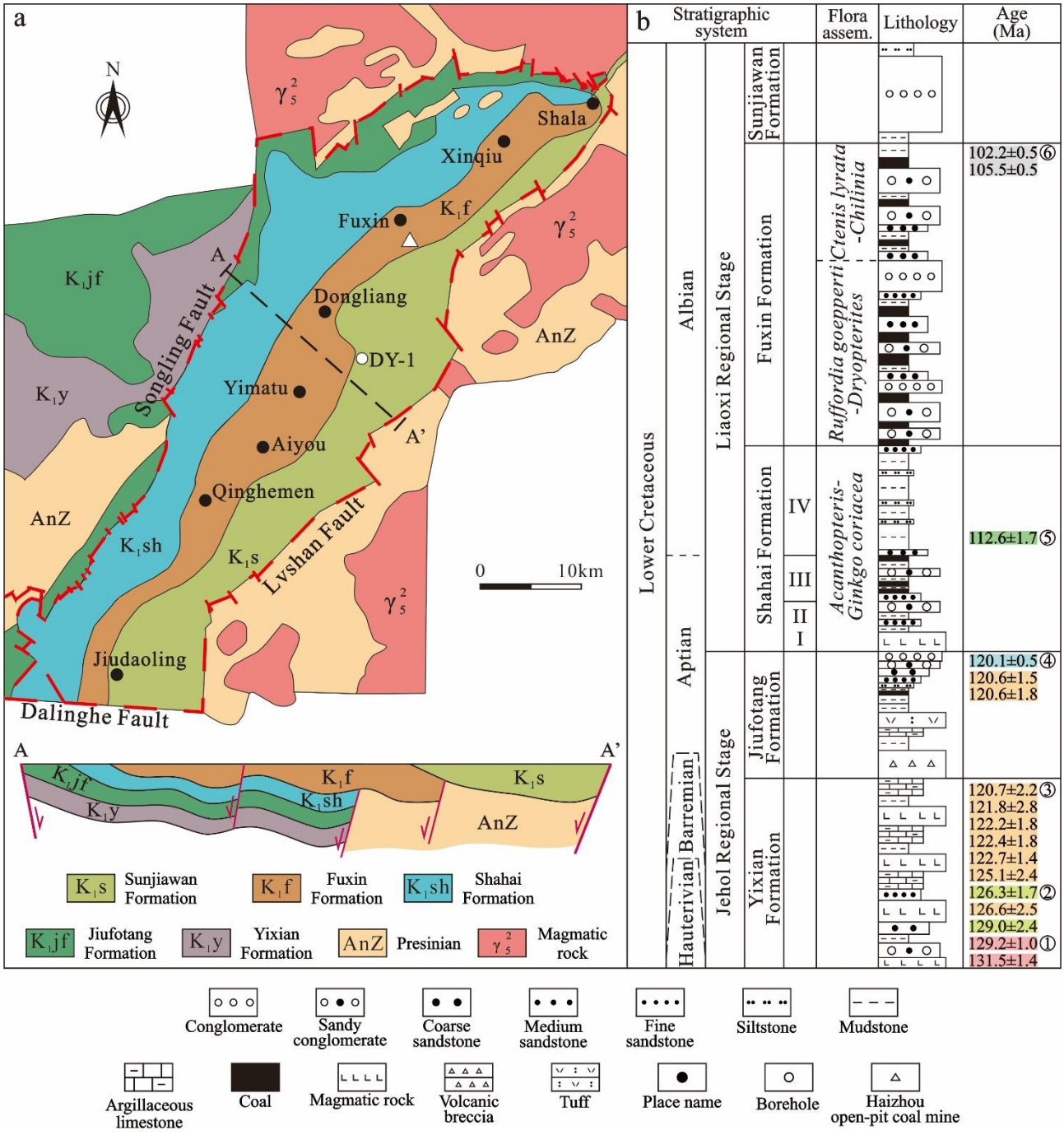
a
N
Shala
Xinqiu
Fuxin
Dongliang
DY-1
Yimatu
Aiyou
Qinghemen
Jiudaoling
Songling Fault
Lvshan Fault
Dalinghe Fault
A
A'
0
10km
AnZ
Sunjiawan Formation
Fuxin Formation
Shahai Formation
Jiufotang Formation
Yixian Formation
Presinian
Magmatic rock
b
Stratigraphic system
Lower Cretaceous
Albian
Aptian
Barremian
Hauterivian
Liaoxi Regional Stage
Jehol Regional Stage
Flora assem.
Lithology
Age (Ma)
Ruffordia goepperti -Dryopterites
Ctenis lyrata -Chilinia
Acanthopteris-Ginkgo coriacea
102.2±0.5⑥
105.5±0.5
112.6±1.7⑤
120.1±0.5④
120.6±1.5
120.6±1.8
120.7±2.2③
121.8±2.8
122.2±1.8
122.4±1.8
122.7±1.4
125.1±2.4
126.3±1.7②
126.6±2.5
129.0±2.4
129.2±1.0①
131.5±1.4
Sunjiawan Formation
Fuxin Formation
Shahai Formation
Jiufotang Formation
Yixian Formation
Presinian
Magmatic rock
Conglomerate
Sandy conglomerate
Coarse sandstone
Medium sandstone
Fine sandstone
Siltstone
Mudstone
Argillaceous limestone
Coal
Magmatic rock
Volcanic breccia
Tuff
Place name
Borehole
Haizhou open-pit coal mine

Fig. 3

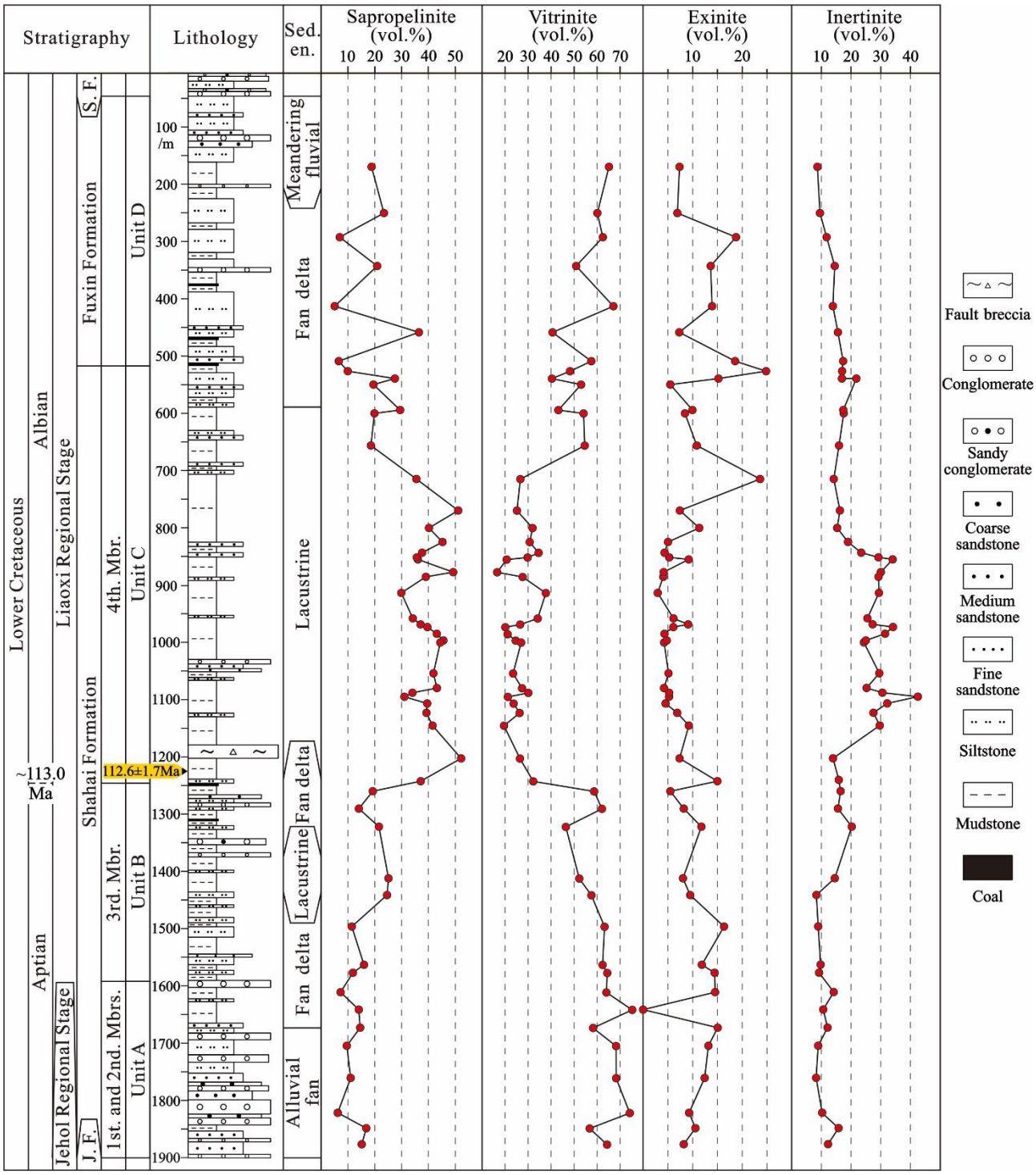
Stratigraphy
Lithology
Sed. en.
Sapropelinite (vol.%)
Vitrinite (vol.%)
Exinite (vol.%)
Inertinite (vol.%)
Lower Cretaceous
Albian
Aptian
~113.0 Ma
Liaoxi Regional Stage
Jehol Regional Stage
Fuxin Formation
Shahai Formation
J. F.
S. F.
1st. and 2nd. Mbrs.
3rd. Mbr.
4th. Mbr.
Unit A
Unit B
Unit C
Unit D
112.6±1.7Ma
Meandering fluvial
Fan delta
Lacustrine
Fan delta
Lacustrine
Fan delta
Alluvial fan
Fault breccia
Conglomerate
Sandy conglomerate
Coarse sandstone
Medium sandstone
Fine sandstone
Siltstone
Mudstone
Coal

Fig. 4

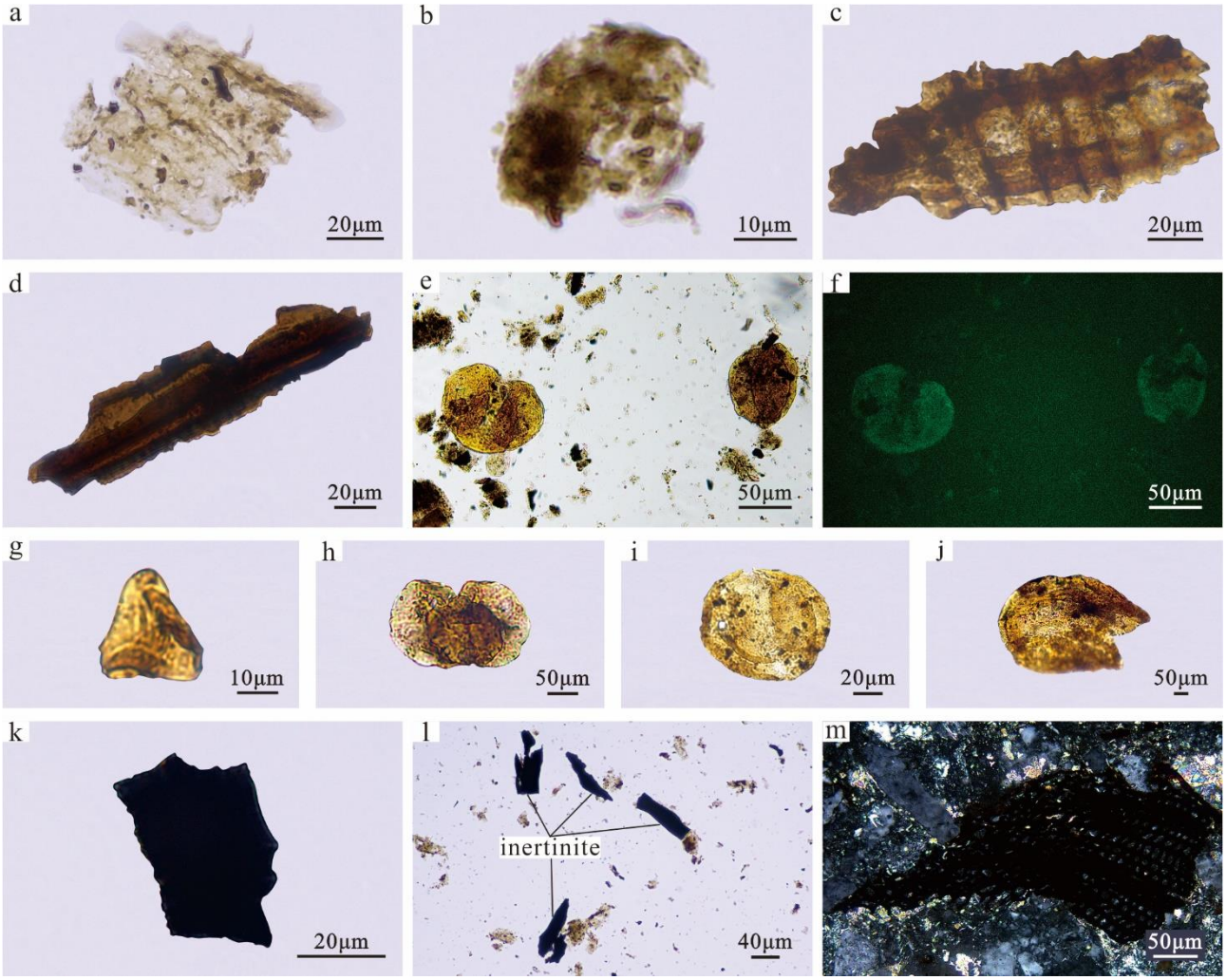
a
20μm
b
10μm
c
20μm
d
20μm
e
50μm
f
50μm
g
10μm
h
50μm
i
20μm
j
50μm
k
20μm
l
inertinite
40μm
m
50μm

Fig. 5

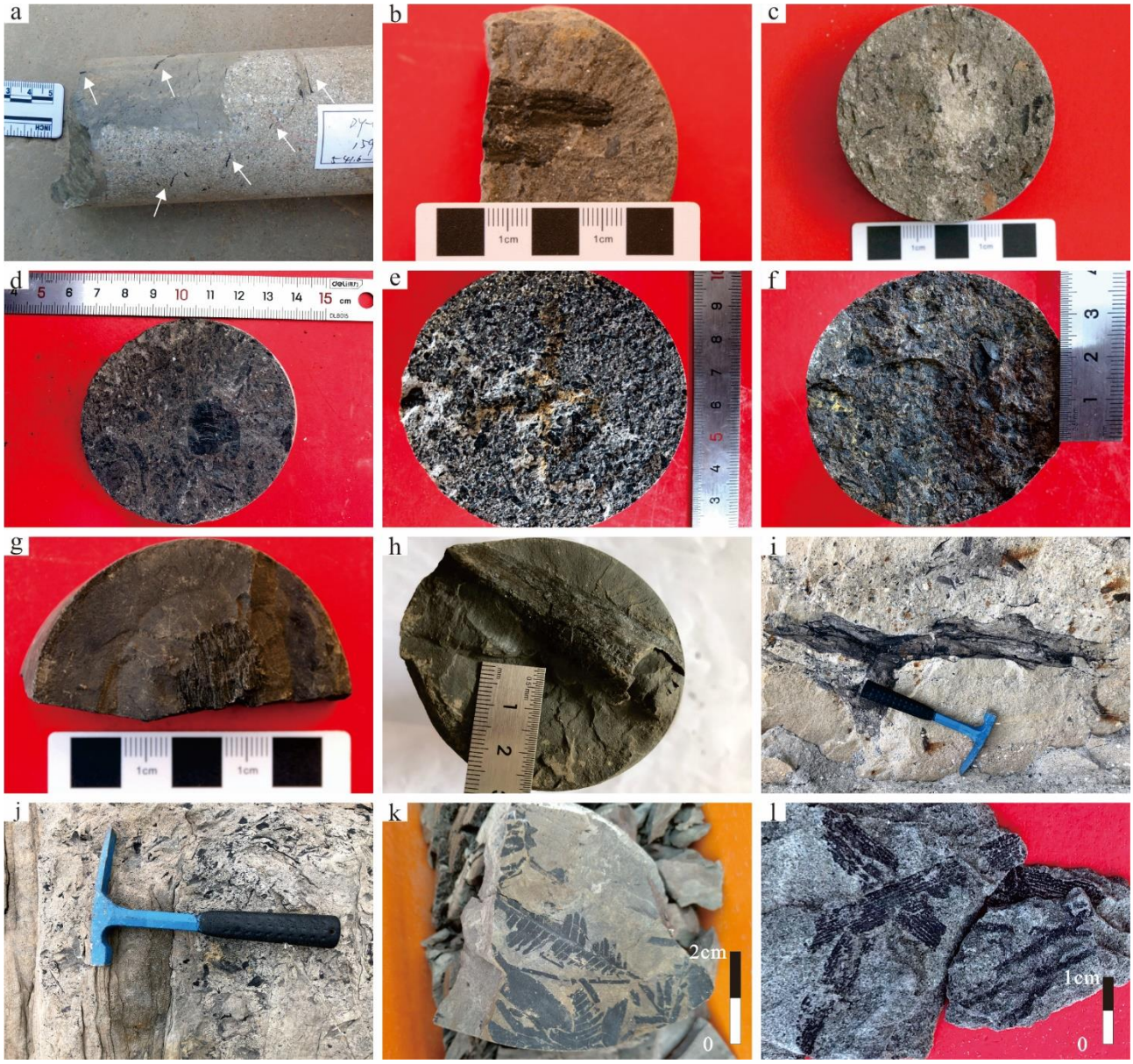
a
b
1cm
1cm
c
d
5 6 7 8 9 10 11 12 13 14 15 cm
e
f
g
1cm
1cm
h
i
j
k
2cm
0
l
1cm
0

Fig. 6

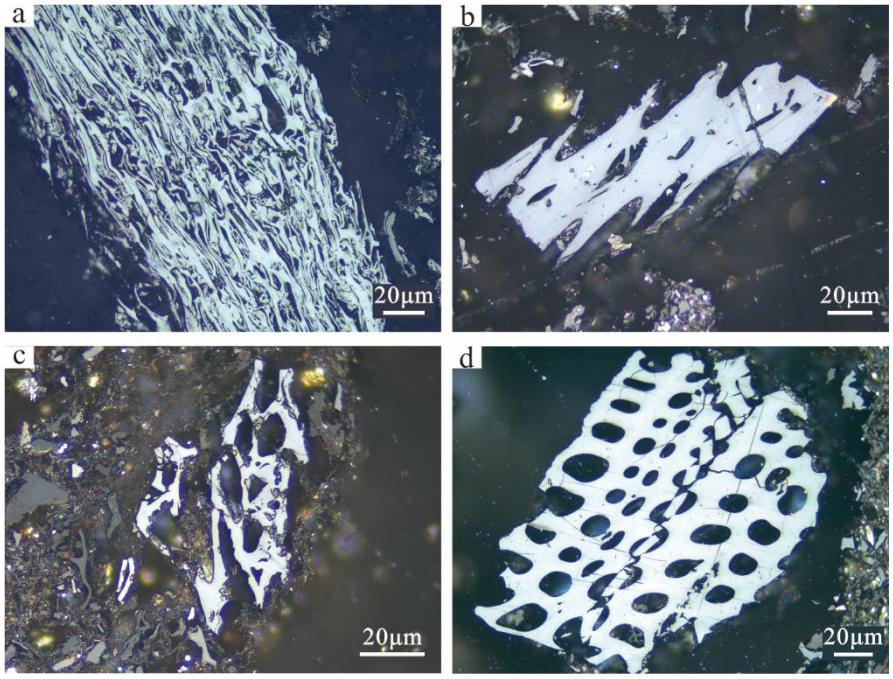

Fig. 7

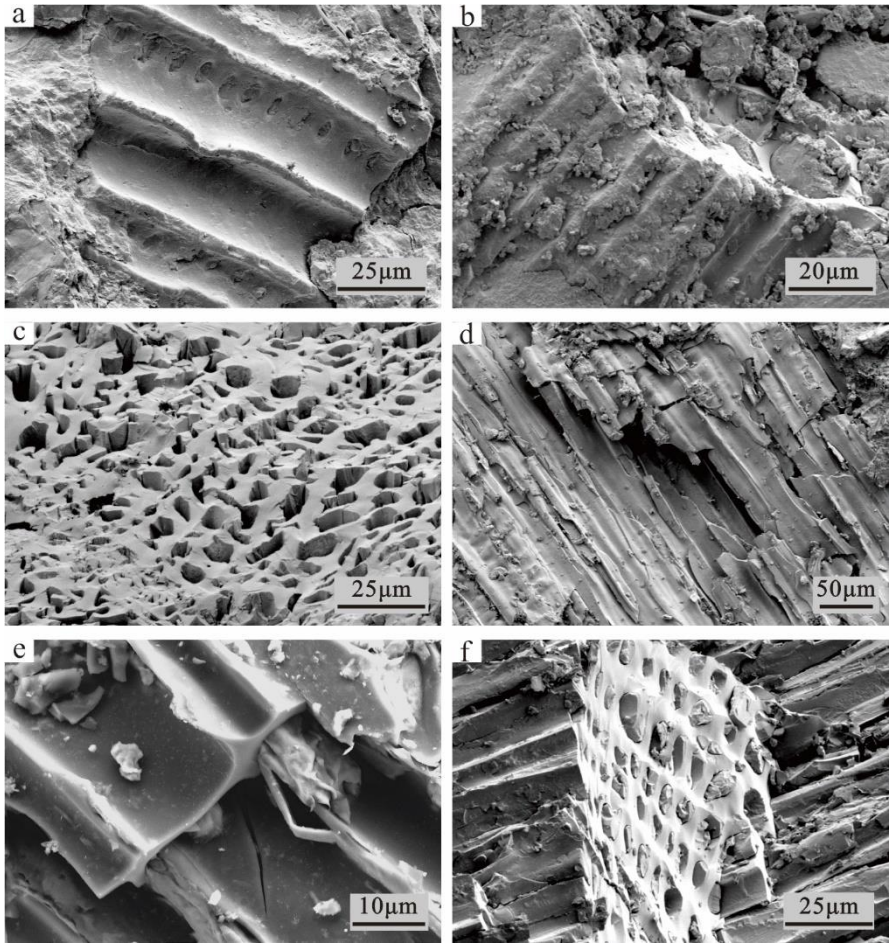

Fig. 8

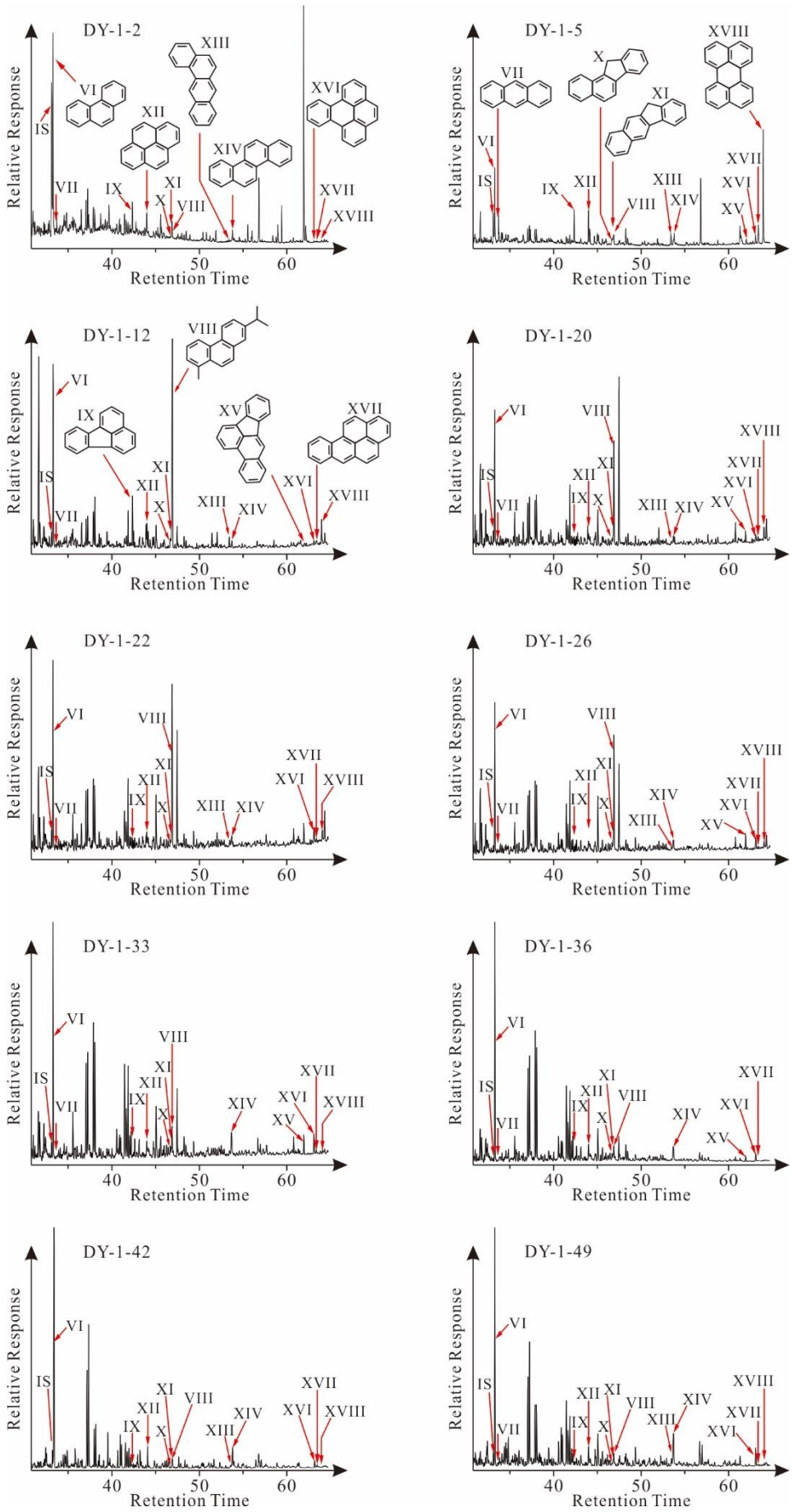
DY-1-2
DY-1-5
DY-1-12
DY-1-20
DY-1-22
DY-1-26
DY-1-33
DY-1-36
DY-1-42
DY-1-49
Relative Response
Retention Time
40
50
60
IS
VI
VII
VIII
IX
X
XI
XII
XIII
XIV
XV
XVI
XVII
XVIII

Fig. 9

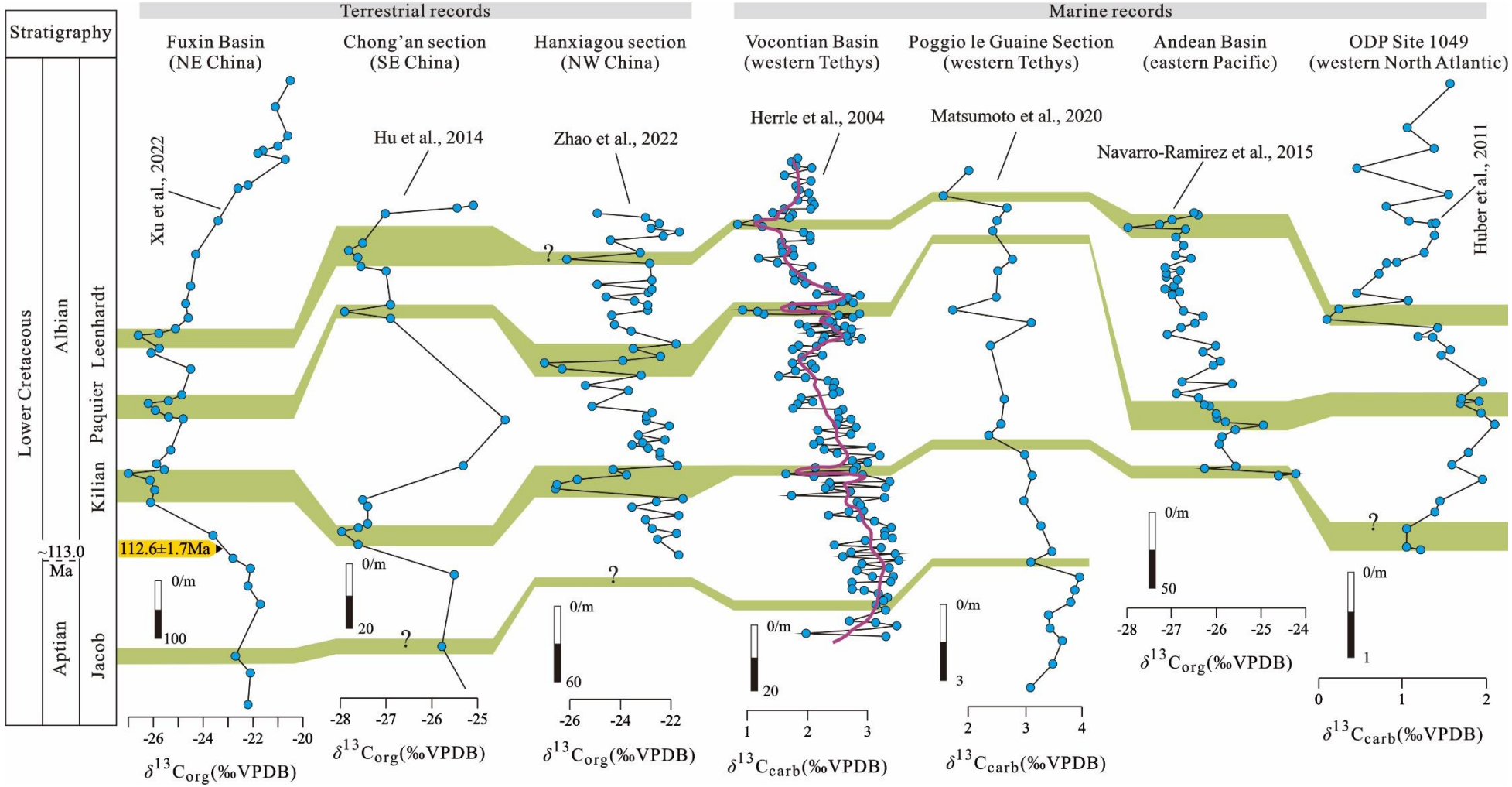
Stratigraphy
Lower Cretaceous
Albian
Aptian
Leenhardt
Paquier
Kilian
Jacob
~113.0 Ma
Terrestrial records
Marine records
Fuxin Basin (NE China)
Chong'an section (SE China)
Hanxiagou section (NW China)
Vocontian Basin (western Tethys)
Poggio le Guaine Section (western Tethys)
Andean Basin (eastern Pacific)
ODP Site 1049 (western North Atlantic)
Xu et al., 2022
Hu et al., 2014
Zhao et al., 2022
Herrle et al., 2004
Matsumoto et al., 2020
Navarro-Ramirez et al., 2015
Huber et al., 2011
112.6±1.7Ma
0/m
100
20
60
3
50
1
δ13Corg(‰VPDB)
δ13Ccarb(‰VPDB)

Fig. 10

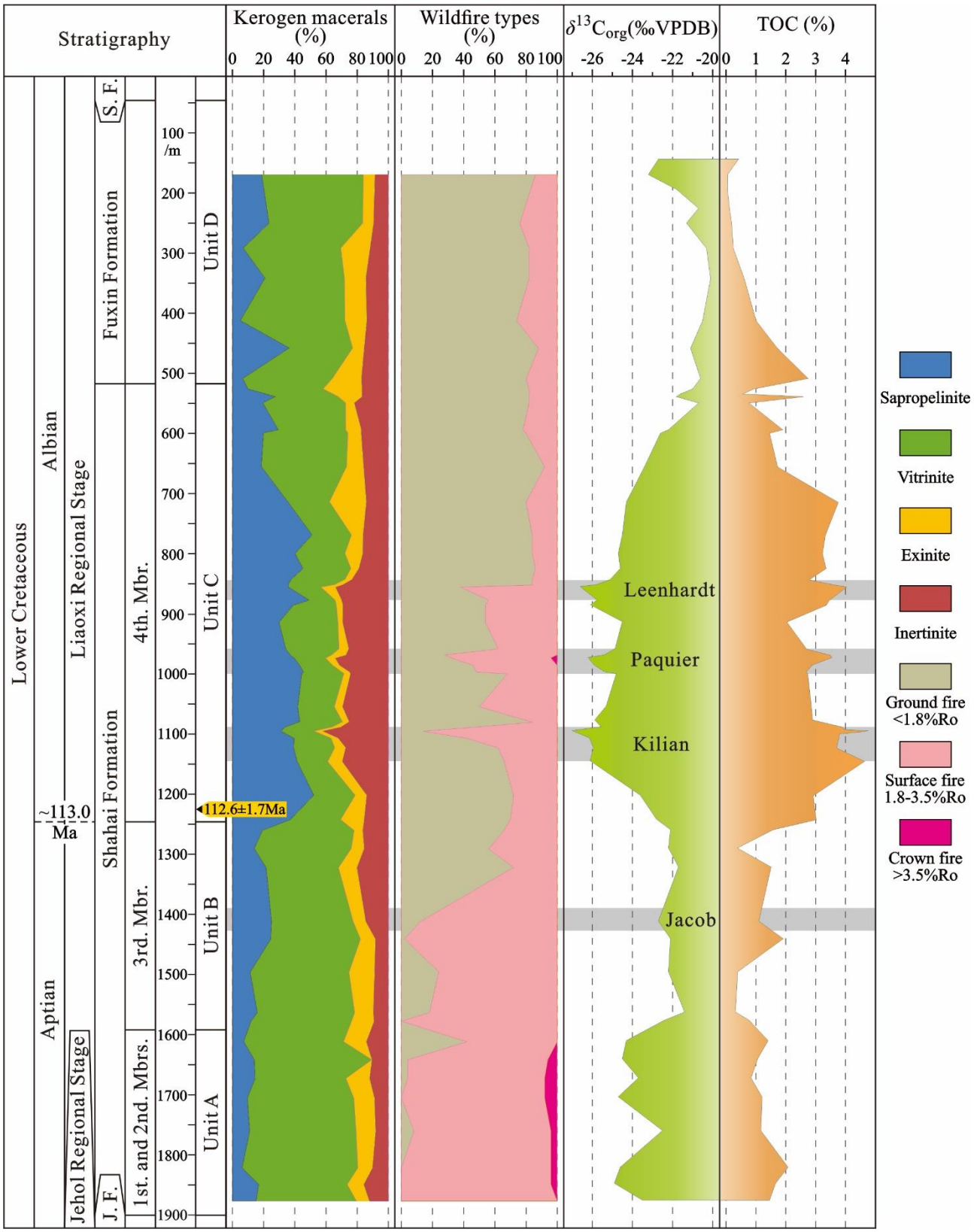
Stratigraphy
Kerogen macerals (%)
Wildfire types (%)
δ13Corg(‰VPDB)
TOC (%)
Lower Cretaceous
Albian
Aptian
Liaoxi Regional Stage
Jehol Regional Stage
S. F.
Fuxin Formation
J. F.
Shahai Formation
4th. Mbr.
3rd. Mbr.
1st. and 2nd. Mbrs.
Unit D
Unit C
Unit B
Unit A
~113.0 Ma
112.6±1.7Ma
Leenhardt
Paquier
Kilian
Jacob
Sapropelinite
Vitrinite
Exinite
Inertinite
Ground fire <1.8%Ro
Surface fire 1.8-3.5%Ro
Crown fire >3.5%Ro

Fig. 11

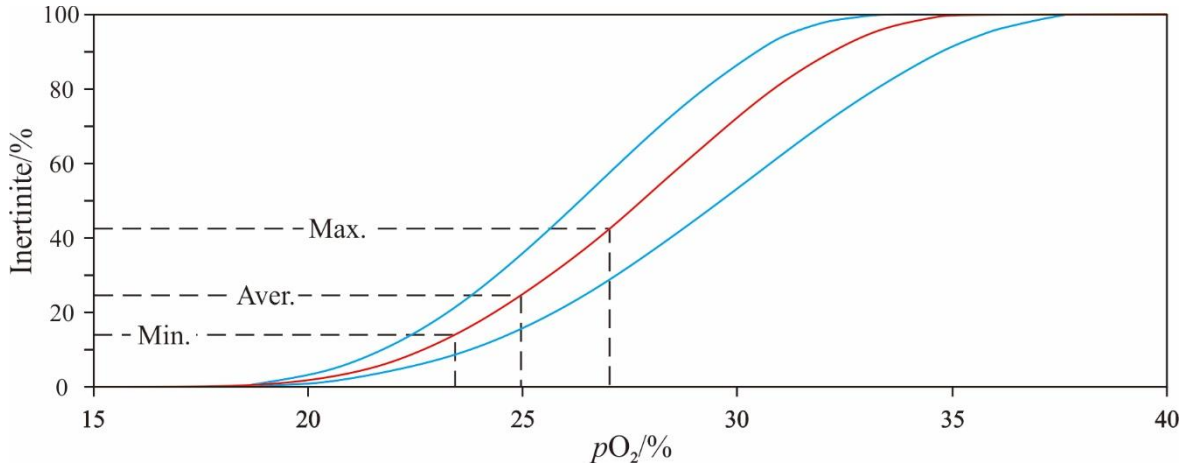

Fig. 12

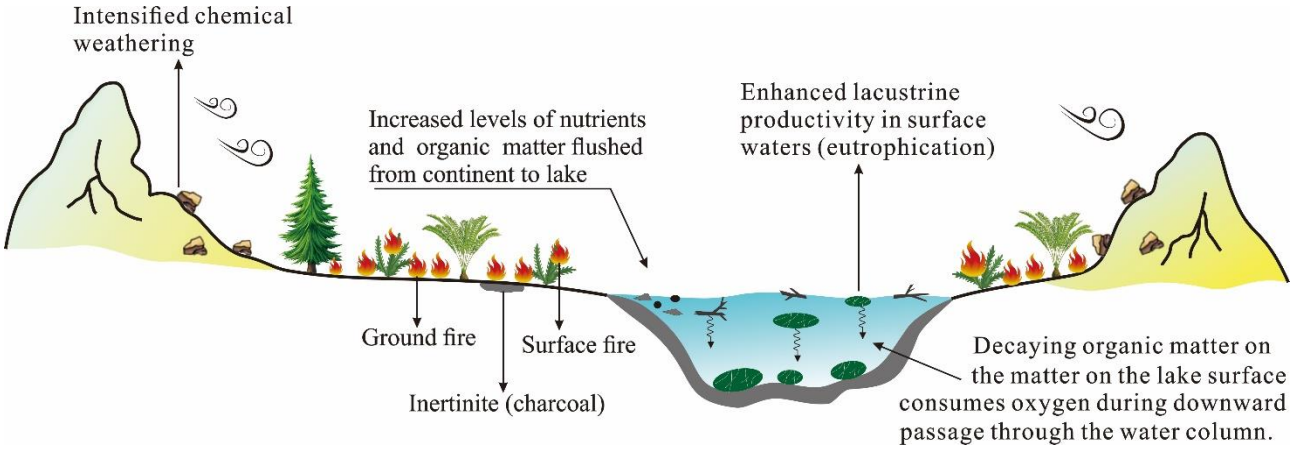
Intensified chemical weathering
Increased levels of nutrients and organic matter flushed from continent to lake
Enhanced lacustrine productivity in surface waters (eutrophication)
Ground fire
Surface fire
Inertinite (charcoal)
Decaying organic matter on the matter on the lake surface consumes oxygen during downward passage through the water column.

Table 1

Organic carbon isotope ($\delta^{13}C_{org}$), total organic carbon (TOC), kerogen macerals and inertinite reflectance values of mudstone samples from the Lower Cretaceous Shahai and Fuxin formations in the Fuxin Basin.

Borehole	Sample	Depth/m	$\delta^{13}C_{org}$	TOC	Kerogen macerals (vol.%, mmf)				Inertinite reflectance (%Ro)		
			‰VPD	%	Sap.	Vitr.	Exi.	Iner.	Min.	Max.	Aver.
	DY-1-1	144	-22.7	0.42	-	-	-	-	-	-	-
	DY-1-2	170	-23.2	0.05	18.8	65.1	7.3	8.7	0.9	2.4	1.4
	DY-1-3	194.6	-21.8	0.05	-	-	-	-	-	-	-
	DY-1-4	225.5	-20.7	0.12	-	-	-	-	-	-	-
	DY-1-5	251	-21.3	0.19	23.4	60.1	6.9	9.6	1.2	2.1	1.7
	DY-1-6	292.6	-20.3	0.25	6.9	62.5	18.8	11.8	0.8	2.2	1.4
	DY-1-7	342.7	-20.1	0.61	20.9	50.9	13.6	14.5	0.9	2.2	1.4
	DY-1-8	413	-20.5	1.01	5.1	67.1	13.9	13.9	1.0	2.5	1.6
	DY-1-9	459	-21.1	1.72	36.5	40.6	7.3	15.6	1.1	2.3	1.6
	DY-1-10	509.5	-20.6	2.75	6.6	57.5	18.6	17.4	0.9	2.6	1.6
	DY-1-11	527	-21.0	0.93	9.9	48.2	24.8	17.0	1.1	2.1	1.6
	DY-1-12	535	-21.6	0.57	-	-	-	-	-	-	-
	DY-1-13	540	-21.8	2.59	27.5	40.4	15.2	17.0	0.6	2.0	1.3
	DY-1-14	549.5	-20.7	0.77	19.5	53.0	5.5	22.0	0.9	2.0	1.4
	DY-1-15	594.5	-22.2	1.90	29.5	43.2	10.0	17.4	0.8	2.4	1.5
	DY-1-16	600	-22.6	1.46	19.9	54.1	8.4	17.5	0.8	2.1	1.4
	DY-1-17	656	-23.4	1.73	18.6	54.6	10.8	16.0	1.0	2.0	1.4
	DY-1-18	714.5	-24.3	3.76	35.5	26.6	23.6	14.2	0.8	2.1	1.4
	DY-1-19	769.5	-24.5	3.33	51.1	25.2	7.4	16.3	0.8	2.3	1.6
	DY-1-20	800	-24.7	3.23	40.2	32.0	11.3	16.5	1.1	2.3	1.5
	DY-1-21	824.9	-24.6	3.34	45.3	30.7	5.0	19.0	1.1	2.4	1.5
	DY-1-22	843.3	-25.1	2.79	37.7	34.6	4.3	23.5	0.9	2.2	1.5
	DY-1-23	852.2	-25.8	3.65	35.7	29.8	5.3	29.2	1.2	2.7	1.6
	DY-1-24	856	-26.6	4.05	36.1	20.7	9.2	34.0	1.5	2.9	1.9
	DY-1-25	877.7	-25.7	3.45	49.2	16.6	4.1	30.1	1.4	2.5	1.8
	DY-1-26	886	-26.1	3.36	39.0	27.6	4.1	29.3	1.2	2.8	1.8
	DY-1-27	914.5	-24.5	2.04	29.9	37.7	2.9	29.4	1.1	2.4	1.8
	DY-1-28	958.5	-24.9	2.70	34.2	34.2	6.1	25.5	1.2	2.9	1.8
	DY-1-29	968.6	-25.4	3.49	37.1	26.6	9.1	27.3	1.0	2.9	2.1
	DY-1-30	974	-26.2	3.55	39.6	20.1	6.1	34.1	1.2	3.8	2.3
	DY-1-31	985.9	-25.9	2.89	43.1	21.1	4.3	31.5	1.2	2.8	1.9
	DY-1-32	997	-25.4	2.69	45.6	24.6	4.8	25.0	1.3	2.9	1.8
	DY-1-33	1000	-24.8	2.74	44.4	27.0	4.2	24.3	0.9	2.5	1.8
	DY-1-34	1055	-25.3	2.86	41.9	23.5	5.1	29.5	0.9	2.6	1.8
	DY-1-35	1080.4	-25.9	2.90	43.2	27.4	4.2	25.3	1.3	2.4	1.7
	DY-1-36	1088.3	-25.6	3.92	34.1	30.1	5.2	30.6	1.0	3.0	1.8
	DY-1-37	1095.5	-27.0	4.76	31.0	21.2	5.2	42.5	1.7	3.3	2.3
	DY-1-38	1107.5	-26.1	3.78	39.5	23.7	4.5	32.2	1.4	3.0	2.1
	DY-1-39	1123.3	-25.9	3.70	39.3	26.3	6.9	27.5	1.3	2.6	1.8

DY-1-40	1146	-26.1	4.64	41.5	19.6	9.2	29.7	1.1	3.0	1.8
DY-1-41	1202.5	-23.6	2.92	52.2	26.5	7.4	14.0	1.3	2.3	1.7
DY-1-42	1242.3	-22.8	3.02	37.1	32.2	15.0	15.6	1.3	2.3	1.7
DY-1-43	1260.4	-22.1	1.58	19.3	58.7	5.5	16.5	1.1	2.8	1.8
DY-1-44	1291.2	-22.2	0.38	14.1	62.1	8.2	15.6	0.8	2.6	1.8
DY-1-45	1322.3	-21.7	1.51	21.6	46.4	11.8	20.3	0.8	2.6	1.6
DY-1-46	1412.5	-22.7	1.10	25.1	52.3	8.0	14.6	1.6	3.4	2.2
DY-1-47	1441.2	-22.1	1.92	24.6	57.5	9.5	8.4	1.8	3.4	2.6
DY-1-48	1496.3	-22.2	0.40	11.4	63.3	16.3	9.0	0.8	3.3	2.0
DY-1-49	1563.8	-21.4	0.32	16.0	62.4	11.9	9.8	1.0	3.3	2.2
DY-1-50	1578	-22.4	0.78	11.9	64.4	14.4	9.3	1.8	3.1	2.4
DY-1-51	1612	-24.3	1.41	7.3	64.0	14.5	14.2	1.0	3.0	1.9
DY-1-52	1642	-24.5	1.06	14.0	75.3	0.0	10.7	1.6	4.3	2.6
DY-1-53	1673.3	-23.7	0.84	14.6	58.3	15.0	12.1	1.8	3.8	2.6
DY-1-54	1705.3	-24.7	1.21	9.6	68.3	13.2	9.0	2.0	3.7	2.8
DY-1-55	1761	-22.5	1.17	11.0	68.3	12.4	8.3	1.7	3.6	2.5
DY-1-56	1821.6	-24.6	2.08	6.2	74.2	9.3	10.3	1.8	4.1	2.6
DY-1-57	1849.3	-24.9	1.66	16.8	56.8	10.6	15.8	1.8	3.6	2.4
DY-1-58	1876.8	-23.5	1.46	15.2	64.3	8.2	12.3	2.0	3.2	2.6

Abbreviations: Iner. = inertinite; Vitr. = vitrinite; Exi. = exinite; Sap. = sapropelinite. Min. = minimum; Max. = maximum; Aver. = average; mmf = mineral matter free.

Table 2

Concentration of the PAHs of ten mudstones from the early Cretaceous Fuxin Basin.

Number	Compound name	Sample number / Concentration of PAHs (μg/g mudstone)									
		DY-1-5	DY-1-8	DY-1-16	DY-1-24	DY-1-26	DY-1-30	DY-1-37	DY-1-40	DY-1-46	DY-1-53
IS	D10-Phenanthrene	0.04141	0.04515	0.02849	0.11199	0.07819	0.07426	0.14018	0.04184	0.15060	0.03929
I	Naphthalene	0.00001	0	0	0	0	0.00399	0	0.00147	0	0
II	Fluorene	0.00061	0.00350	0.01169	0.02711	0.02077	0.03674	0.03862	0.04673	0.03681	0.05182
III	Biphenyl	0.00001	0	0.00294	0.01860	0.00612	0.04734	0.01910	0.09328	0	0.00508
IV	Dibenzothiophene	0.00216	0.00575	0.01254	0.03321	0.03150	0.07033	0.08076	0.11306	0.17462	0.05195
V	Dibenzofuran	0.00037	0.00815	0.09972	0.26086	0.12739	0.29177	0.17239	0.23040	0.00313	0.03044
VI	Phenanthrene	0.05655	0.12072	0.33174	0.88579	0.67586	1.31083	2.03635	2.72338	2.20779	0.75873
VII	Anthracene	0.00110	0.00300	0.00225	0.00275	0.00440	0.00368	0.00166	0.00436	0	0.00913
VIII	Retene	0.00158	0.00423	0.12800	0.21727	0.18751	0.30194	0.08485	0.04924	0.00130	0.01169
IX	Fluoranthene	0.00917	0.05118	0.09612	0.05740	0.03818	0.05019	0.03035	0.03064	0.04148	0.01406
X	Benzo[a]fluorene	0.00021	0.00340	0.00422	0.00493	0.00374	0.00598	0.00618	0.00597	0.00844	0.00160
XI	Benzo[b]fluorene	0.00068	0.01587	0.02661	0.05715	0.04476	0.07620	0.06073	0.05725	0.06277	0.01849
XII	Pyrene	0.00695	0.05776	0.04693	0.07843	0.06009	0.09071	0.13335	0.17908	0.19042	0.06031
XIII	Benz(a)anthracene	0.00027	0.01811	0.01818	0.00485	0.00324	0.00216	0	0	0.00718	0.00259
XIV	Chrysene	0.00044	0.01326	0.01484	0.05154	0.04669	0.10972	0.23315	0.21152	0.24639	0.12779
XV	Benzofluoranthenes	0	0.00264	0.00134	0.00363	0	0.00624	0.00853	0.00319	0	0
XVI	Benzo(e)pyrene	0.00040	0.01185	0.00659	0.04256	0.04892	0.08219	0.15981	0.09193	0.06859	0.05603
XVII	Benzo(a)pyrene	0.00037	0.02997	0.00485	0.00733	0.00671	0.00775	0.00714	0.00426	0.00550	0.00197
XVIII	Perylene	0.00053	0.18778	0.04626	0.00069	0.00032	0.00076	0.00179	0	0.00028	0.00049
Total PAHs (more than 3-ring)		0.07825	0.51976	0.72792	1.41431	1.12043	2.04836	2.76389	3.36081	2.84014	1.06287